arXiv:1703.10946v1 [physics.comp-ph] 31 Mar 2017

Dynamical structure of entangled polymers simulated under shear flow

Airidas Korolkovas,[*,†,‡,¶] Philipp Gutfreund,[†] and Max Wolff[¶]

†*Institut Laue-Langevin, 71 rue des Martyrs, 38000 Grenoble, France*

‡*Université Grenoble Alpes, Liphy, 140 Rue de la Physique, 38402 Saint-Martin-d'Hères, France*

¶*Division for Material Physics, Department for Physics and Astronomy, Lägerhyddsvägen 1, 752 37 Uppsala, Sweden*

E-mail: korolkovas@ill.fr

April 3, 2017

Abstract

The non-linear response of entangled polymers to shear flow is complicated. Its current understanding foots mainly on a rheological description in terms of the complex viscosity. However, the full picture requires an assessment of the dynamical structure of individual polymer chains which give rise to the macroscopic observables. Here we shed new light on this problem, using a novel computer simulation based on a blob model, suitable to describe polymer melts and semi-dilute solutions. We examine the stress fluctuation and diffusion spectra during a steady shear flow. The relaxation dynamics are found to speed up along the flow direction, but slow down along the shear gradient direction. The third axis, vorticity, shows a slowdown at the short scale of a tube, but reaches a net speedup at the large scale of the chain radius of gyration.

Introduction

Entangled polymers are a network of long, interpenetrating chains, as illustrated in Fig. 1. The motion is driven by random thermal fluctuations, while the excluded volume interaction prevents the chains from crossing each other. The resulting dynamics display a rich variety of phenomena, distinct from most other materials. Despite its macroscopically complicated behaviour, the physics of the entangled network is mostly governed by one parameter: the number of chain segments N. Temperature,[1] concentration,[2,3] or even chemical composition,[4] typically do not influence the macroscopic properties, but only result in a shift of the relevant time and length scales. This universality is appealing, since it suggests that most of polymer physics might be described in terms of one fundamental model, perhaps containing only one parameter, the chain length N.

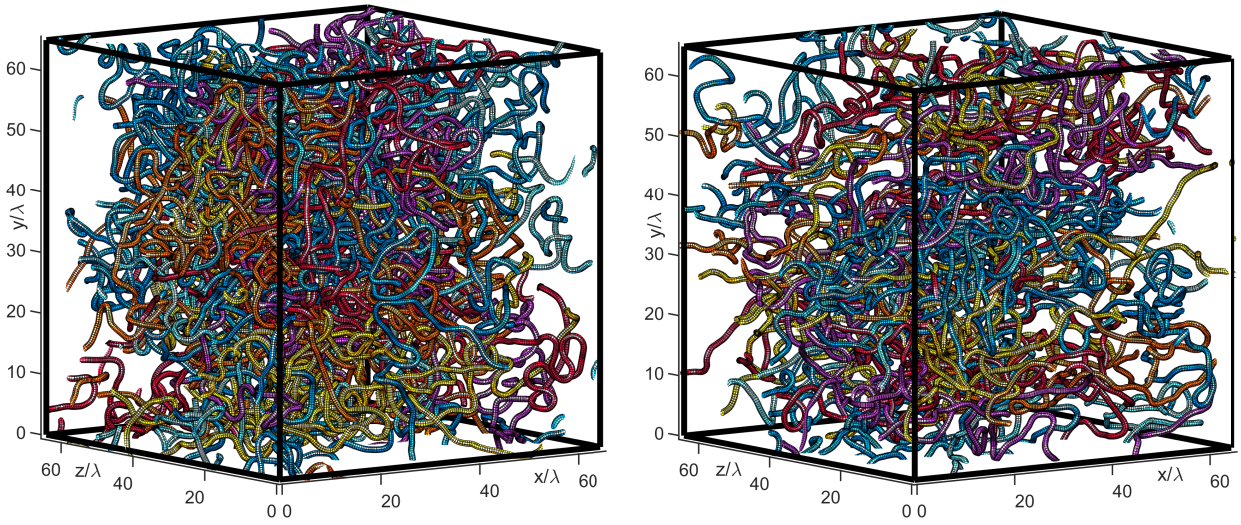

Figure 1: Simulation snapshot in 3D: a) static, b) shear Wi = 32. Number of chains $C = 64$, blobs per chain $N = 512$. Individual chains are colored in one of seven randomly chosen colors.

For monodisperse systems it might be sufficient to evaluate the dynamics of a single chain immersed in the averaged confining field of all the other chains. Such mean field approximations have been developed extensively for entangled polymers, with the most notable one being the Reptation Theory by de Gennes,[5] Doi and Edwards.[6] It is formulated in terms of a

stochastic differential equation for the shape $\mathbf{R}(t,n)$ of a continuous path indexed $0 < n < N$ at time t. The solution of the equation provides in principle any correlation of interest, and thereby any physical observable. Its most famous result is the law for the mean squared displacement of the central monomer:

$$g_1(t) = \langle [\mathbf{R}(t, N/2) - \mathbf{R}(0, N/2)]^2 \rangle \propto t^{1/4}, \quad \left(\tau_e = \tau N_e^2\right) \ll t \ll \left(\tau_R = \tau N^2\right) \tag{1}$$

with $N_e \approx 50$ the minimum chain length to form one entanglement, and τ the unit of time. This behaviour is in stark contrast[7] to random jump diffusion $g_1 \propto t$, or the Rouse[8] dynamics: $g_1 \propto t^{1/2}$, which also predict the longest relaxation time to be $\tau_R = \tau N^2$, while the entanglement prediction[9] is $\tau_d = \tau (N/N_e)^{3.4}$.

Theories and structural dynamics experiments[10–15] of entangled polymers have mostly been limited to equilibrium. In contrast, the practical and industrial use of entangled polymers usually involves shear flow, for example in food thickeners,[16] paint formulations,[17] plastics injection[18] and extrusion,[19] fibre spinning,[20] and enhanced oil recovery from shale rock.[21] Non-equilibrium entanglement dynamics also play a role in biology, such as the cytoskeleton[22] during cell division, and the cartilage[23] during joint movement.

When the applied shear rate $\dot{\gamma} = dv_x/dy$ exceeds the inverse polymer relaxation time,

$$\text{Weissenberg number} = \text{Wi} = \dot{\gamma}\tau_d \gtrsim 1 \tag{2}$$

a non-linear flow regime is entered. In rheology one observes[24] a drop of viscosity (shear thinning), and the emergence of normal stress differences (Weissenberg effect). Small angle neutron scattering (SANS) experiments have established[25–32] that the shear thinning is accompanied by a stretching of the chains along the shear flow, and a collapse along the vorticity. Neutron reflectometry was used to measure the chain collapse along the shear gradient.[33,34] From superposition rheology measurements a large speedup of relaxation dynamics along the flow and vorticity was reported.[35] Dielectric spectroscopy data shows a

slight slowdown of the dynamics along the shear gradient.[36] Neutron spin echo (NSE) experiments have extracted a clear speedup along the vorticity.[37]

The interpretation of shear experiments can benefit from multi chain computer simulations which do not involve any mean field assumptions and therefore can verify, refute, or complement the effective single chain theories such as the Convective Constraint Release (CCR).[38] Hard beads connected with stiff springs (Kremer-Grest (KG) model[39]) are often used to represent a polymer melt. A coarser model, also suitable for semi-dilute solutions, is based on soft blobs smeared over a continuous backbone.[40] Both methods can reproduce the power law of Eq. (1). While the multi chain simulations are conceptually simple and based on only a few assumptions, they are demanding in terms of computational time. Previous simulations have focused on the average steady-state[41–46] and transient[47] responses. Very little data is available on the non-equilibrium relaxation dynamics, restricted to short unentangled chains at extremely high shear rates[48] unattainable in experiments. Here we provide the simplest possible, yet fast and realistic, approach for the simulation of long polymer chains under shear flow. The source code is available for download from Ref.[49] The single-core CPU version reaches sub-Rouse diffusive behaviour ($g_1/\sqrt{t}$ slope negative) within about a day of computation. The GPU version, written in CUDA, runs at least 10x faster and is competitive with typical supercomputer facilities.

In the first part of the article we describe the physics and mathematics behind our simulation. The accompanying MATLAB code provides the necessary comments to aid in the understanding of the algorithm. In the second part we present results on a polymer melt under shear, in terms of its steady-state response as well as the fluctuations around it, from both structural and mechanical points of view. In the third part we discuss our findings and set them into context with experimental results.

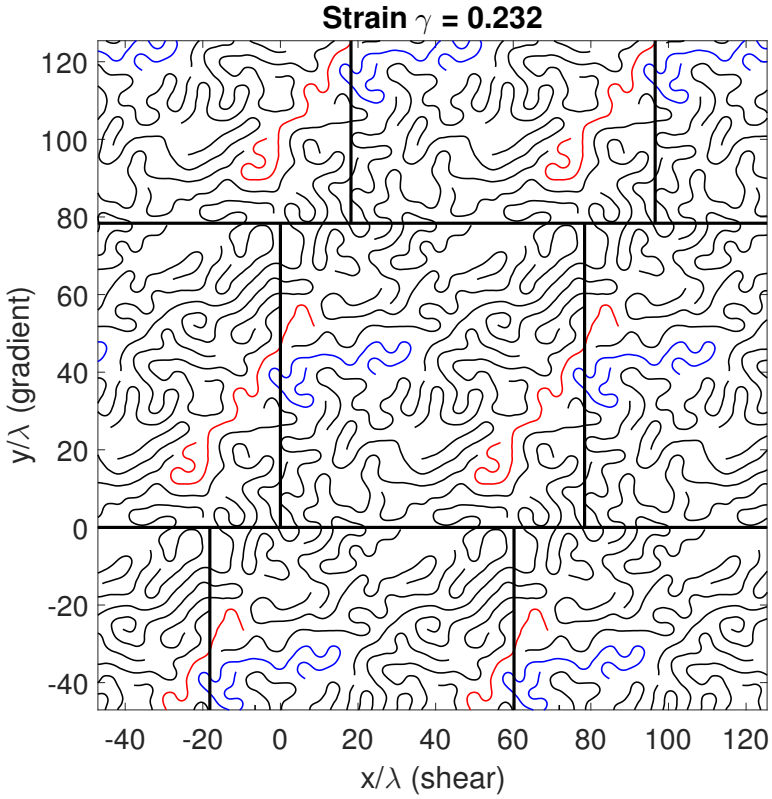

Figure 2: A snapshot of a 2D polymer simulation under shear flow, using Lees-Edwards boundary conditions. Two random chains are colored for clarity.

Simulation method

The simulation is based on a previously published algorithm [40] for equilibrium systems, but now extended for bulk shear flow by imposing a Couette velocity profile:

$$\mathbf{v} = \dot{\gamma} y \mathbf{e}_x. \tag{3}$$

To simulate a bulk shear flow, one has to use the Lees-Edwards boundary conditions,[50] illustrated in Fig. 2. In a cubic box of length L, every particle $\mathbf{R}$ is replicated at points

$$\mathbf{R} \to \mathbf{R} + L[(\gamma n_y + n_x)\mathbf{e}_x + n_y \mathbf{e}_y + n_z \mathbf{e}_z], \tag{4}$$

where the n_x, n_y, and n_z are integers $-\infty$, ..., -1, 0, $+1$ ..., $+\infty$. The strain

$$\gamma(t) = \int_{-\infty}^{t} \dot{\gamma}(t')\, dt' \tag{5}$$

accumulates as the simulation progresses, and the oblique-periodic images can shift many times over their own length. For numerical stability reasons, the strain is always folded to

$$\gamma \to \gamma - \texttt{round}(\gamma) \tag{6}$$

restricting it to the symmetric range $-0.5 < \gamma < 0.5$.

The motion of $c = 1, 2, \ldots, C$ chains, each described by a continuous curve $\mathbf{R}_c(t, s)$, with variables t for time and $0 < s < 1$ as monomer index, is solved numerically. Every chain has N degrees of freedom and follows the stochastic first order equation of motion

$$\zeta \frac{\partial \mathbf{R}_c(t,s)}{\partial t} = \left(\frac{3k_BT}{Nb^2}\right) \frac{\partial^2 \mathbf{R}_c(t,s)}{\partial s^2} \qquad \text{(spring)} \tag{7a}$$

$$+ N \left(\frac{v k_B T}{\lambda^3}\right) \sum_{c'=1}^{C} \int_0^1 ds'\, f[\mathbf{R}_c(t,s) - \mathbf{R}_{c'}(t,s')] \qquad \text{(excluded volume)} \tag{7b}$$

$$+ \zeta \dot{\gamma}\, (\mathbf{R}_c(t,s) \cdot \mathbf{e}_y)\, \mathbf{e}_x \qquad \text{(shear flow)} \tag{7c}$$

$$+ \sqrt{2k_BT\zeta}\, \mathbf{W}_c(t,s) \qquad \text{(thermal noise)} \tag{7d}$$

Here $\zeta = 6\pi\eta_s bN$ is the friction coefficient of the chain center of mass, defining the unit of time:

$$\tau = \frac{6\pi\eta_s b^3}{k_BT}, \tag{8}$$

and the strength of the thermal noise, modeled by a Wiener process $\langle \mathbf{W}_c(t,s)\mathbf{W}_{c'}(t',s')\rangle = \mathbb{I}\,\delta_{cc'}\,\delta(t-t')\,\delta(s-s')$. While mathematically any values are allowed for the chain stiffness λ/b, and the excluded volume strength v/λ^3, here we only consider the case with both parameters equal (or close) to unity, $v = \lambda^3 = b^3$. This corresponds to a semi-dilute polymer solution of density ρ and molecular weight M_w, characterized by the blob size and the number of blobs per chain respectively:[51]

$$\lambda \propto \rho^{-3/4} \quad \text{and} \quad N \propto \rho^{5/4} M_w \tag{9}$$

The model could also be used as a very coarse description of a polymer melt $\rho \to \rho_0$, although in that case the mapping of Eq. (9) does not apply and the absolute values of λ and N depend on the chemical species. We do not take these details into account, but instead focus on the scale significantly larger than the monomer size λ, whose properties are generally the same for all entangled polymers.

The repulsive excluded volume force between two blobs at a distance $\mathbf{r}$ is described[52] by a Gaussian:

$$f(\mathbf{r}) = -\nabla e^{-\mathbf{r}^2/2\lambda^2} = \frac{\mathbf{r}}{\lambda^2} e^{-\mathbf{r}^2/2\lambda^2}. \tag{10}$$

The simulation box is cubic and of fixed volume

$$V = L^3 = v_0 \left(\frac{4\pi}{3}\right) NC\lambda^3 \tag{11}$$

where we choose the numerical prefactor $v_0 = 2$ to allow some freedom of movement for the blobs. To solve Eq. (7) while avoiding chain crossings, we sample each chain with a number of $J \gg N$ points and use the convolution theorem to approximate the excluded volume force

for a particle located at $\mathbf{r}$:

$$\mathbf{F}(\mathbf{r}) = \sum_{c,j=1}^{C,J} f(\mathbf{r} - \mathbf{R}_{c,j}) \tag{12a}$$

$$\approx \texttt{IFFT}\left\{\texttt{FFT}\left[\sum_{c,j=1}^{C,J} \delta(\mathbf{r}' - \mathbf{R}_{c,j})\right] \cdot \texttt{FFT}[f(\mathbf{r}')]\right\} \tag{12b}$$

In the quiescent case the Fourier transforms automatically impose the periodic boundary conditions. Under bulk shear, the Lees-Edwards boundaries are not periodic in the rectangular coordinate system, but they are periodic in the oblique one, making the convolution theorem applicable (see Appendix A). In short, the particle positions are first transformed to the oblique system, then the convolution theorem, Eq. (12b), is applied to find the oblique force, which is then transformed back to the rectangular system where the equation of motion, Eq. (7), is applied.

Results

We have used our code to explore the structural and mechanical changes of entangled polymers under shear flow. We have simulated $C = 64$ chains of length $N = 512$ (see Fig. 1). Seven simulation runs where performed for different Weissenberg numbers $\mathrm{Wi} = \dot{\gamma}\tau_d = 0$, 0.3, 1, 3, 10, 32, and 100, with all other parameters kept fixed. The system is moderately entangled, with about $Z = N/N_e = 8.5$ entanglements per chain at equilibrium.[53] Computations were carried out on an Nvidia Quadro M5000 GPU card for about 4 days per run, generating trajectories of $20\tau_d$ relaxation times each.

The scenarios range from Newtonian to strongly non-linear regimes, where the fluid becomes highly anisotropic. First we summarize the steady state structure under shear, which is well known and serves as a check for the validity of our simulations. Second, we explore diffusion as probed by neutron spin echo and dielectric spectroscopy experiments. Third, the stress fluctuations around the steady state are reported, some of which are accessible by

superposition rheology.

Steady state structure

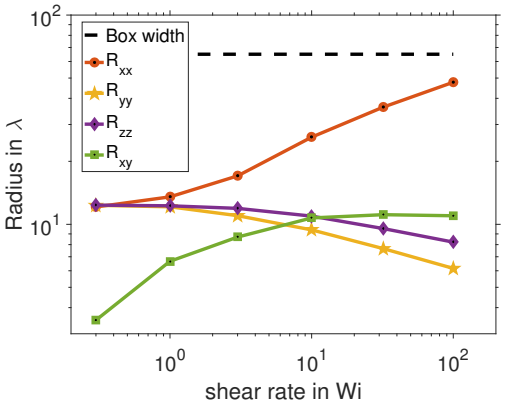

Figure 3: Inertia tensor

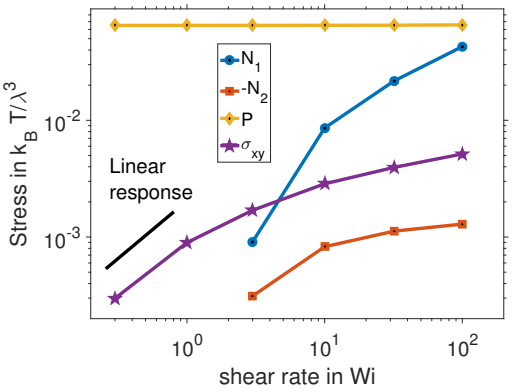

Figure 4: Stress tensor

The radius of gyration squared

$$R_g^2 = \langle (\mathbf{R}_j - \langle \mathbf{R}_j \rangle)^2 \rangle = 2 \sum_{n=1}^{N-1} |\mathbf{a}_n|^2 \propto \lambda^2 N \tag{13}$$

can be expressed in terms of Rouse modes

$$\mathbf{a}_n = \frac{1}{J} \sum_{j=1}^{J} \mathbf{R}_j \cos\left(\frac{\pi(2j-1)n}{2J} \right) \tag{14}$$

and is proportional to the blob size squared and the number of blobs. It becomes a tensor in the non-linear flow regime:

$$R_{\alpha\beta}^2 = 2 \sum_{n=1}^{N-1} (\mathbf{a}_n \cdot \mathbf{e}_\alpha)(\mathbf{a}_n \cdot \mathbf{e}_\beta) \tag{15}$$

The stress on the polymer backbone is described by a similarly defined tensor:

$$\sigma_{\alpha\beta} = \frac{6\pi^2 k_B T}{V N \lambda^2} \sum_{n=1}^{N-1} n^2 (\mathbf{a}_n \cdot \mathbf{e}_\alpha)(\mathbf{a}_n \cdot \mathbf{e}_\beta) \tag{16}$$

Because of the n^2 factor, the stress is more sensitive to shorter length scales (higher Rouse modes), while the radius of gyration is dominated by the largest length scales.

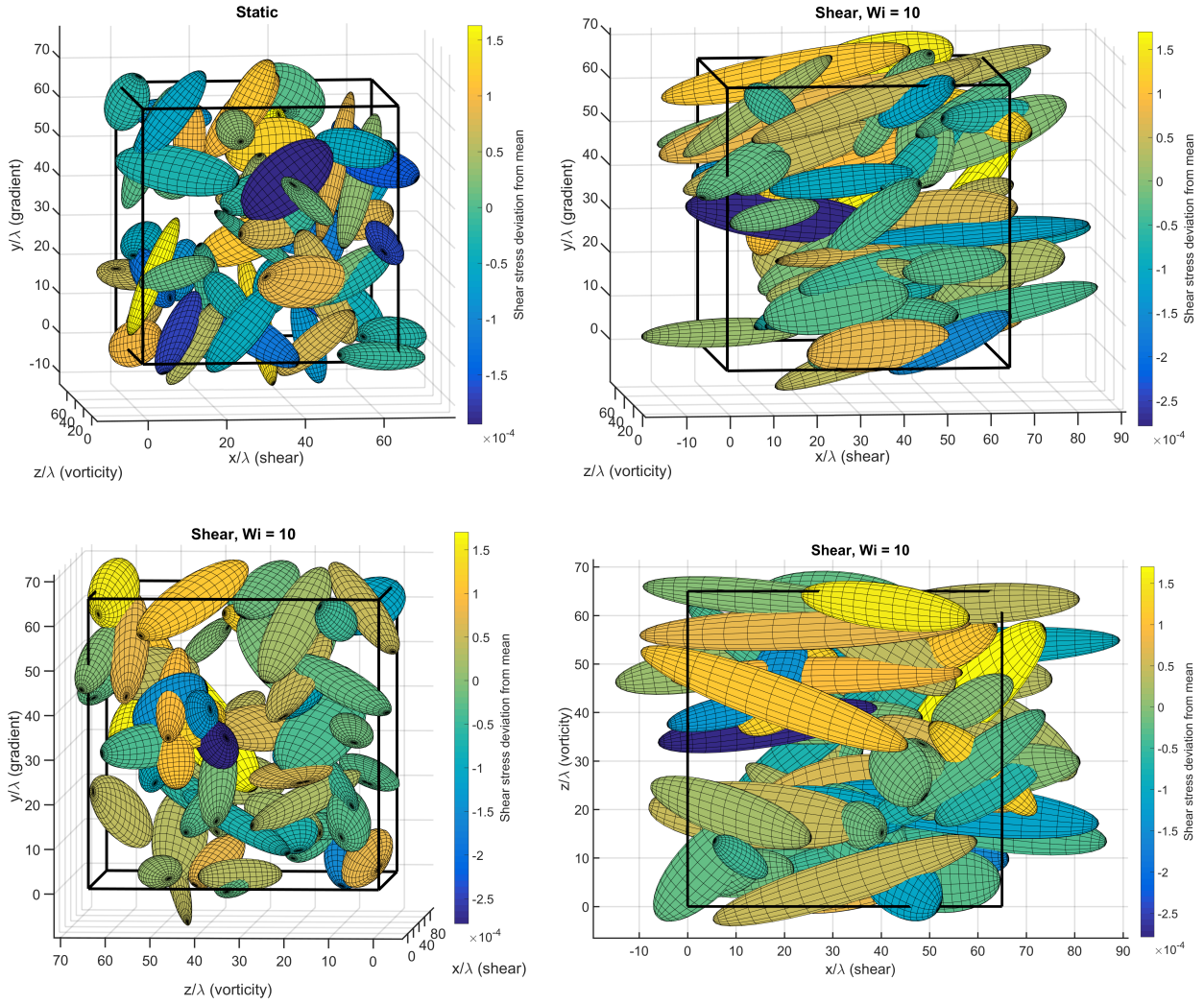

Figure 5: Snapshot of the simulated fluid. The shape of the ellipsoids depicts the chain inertia tensors, and their color shows the shear stress excess from the mean.

Under Couette shear, we have four different non-zero components, shown in Figs. 3 and 4 for the two tensors. For shear rates exceeding Wi = 1, the chains stretch along the flow direction, and shrink along the shear gradient direction, as well as along the vorticity direction but to a lesser extent. In addition, the chain shape is tilted with respect to the flow direction with a significant R_{xy} component emerging under shear. The effective tilt angle θ

can be found by diagonalizing the inertia matrix:

$$\tan 2\theta = \frac{2R_{xy}^2}{R_{xx}^2 - R_{yy}^2} \tag{17}$$

and the principal moments of inertia are

$$R_{\pm}^2 = \frac{1}{2}\left[R_{xx}^2 + R_{yy}^2 \pm \sqrt{\left(R_{xx}^2 - R_{yy}^2\right)^2 + 4R_{xy}^4}\right] \tag{18}$$

For a chain arbitrarily oriented in 3D the matrix can be diagonalized by standard numerical algorithms. The result is shown in Fig. 5. The instantaneous inertia tensors are calculated for each chain, and plotted as an ellipsoid, oriented along the eigenvectors, with the axes representing the eigenvalues, rescaled by a factor of 0.7 for clarity. In Appendix B we report more details on the fluid structure: the form and structure factors, and the distribution of chain centers of mass.

The stress tensor behaves similarly to the inertia tensor. The chain stretching along the flow and collapsing perpendicular to it contributes to the first normal stress difference $N_1 = \sigma_{xx} - \sigma_{yy}$. The collapse in the z (vorticity) direction is smaller than in the y (gradient) direction, which is corroborated by the second normal stress difference $N_2 = \sigma_{yy} - \sigma_{zz}$, observed to be negative. The net pressure $P = (\sigma_{xx} + \sigma_{yy} + \sigma_{zz})/3$ is not affected by flow. The shear stress $\sigma_{xy} = \eta\dot{\gamma}$ is linear at first, but grows slower at higher speeds (shear thinning), similar to the trend in the off-diagonal inertia component R_{xy}.

Diffusion

The mean squared displacement of the central $j = J/2$ monomer

$$g_1(t) = \langle[\mathbf{R}_{J/2}(t) - \mathbf{R}_{J/2}(0)]^2\rangle \tag{19}$$

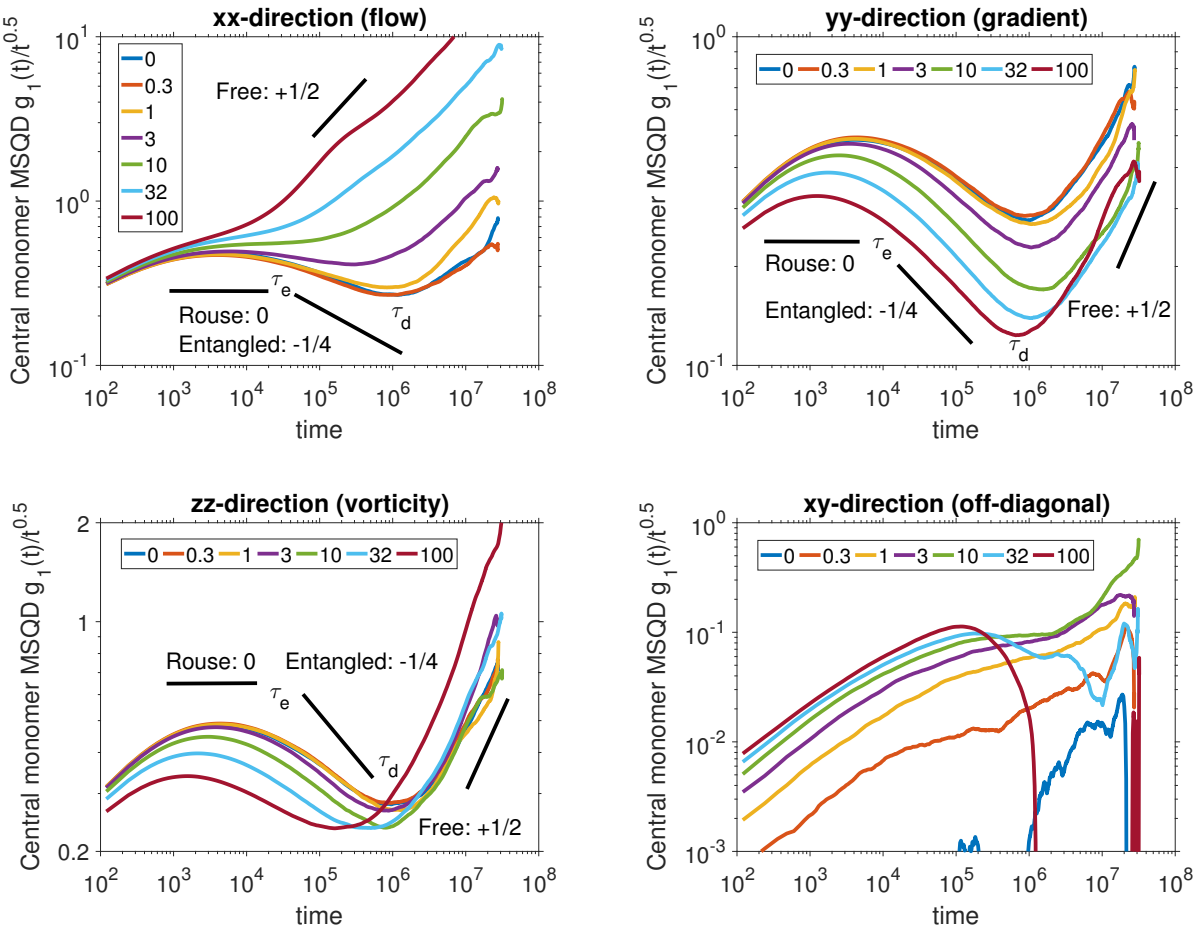

Figure 6: Central monomer diffusion spectrum. The legend indicates shear rate in Wi.

shows a clear signature of entanglement. In particular, $g_1(t)/\sqrt{t}$ has a negative slope for intermediate time scales ($\tau_e = \tau N_e^2$) $\ll t \ll$ ($\tau_R = \tau N^2$), which is sub-Rouse behaviour, resulting from reptation in the presence of contour length fluctuations. The pure reptation regime without fluctuations, $\tau_R \ll t \ll \tau_d$, is only expected to emerge for extremely long chains $N \gtrsim N_e^3 \approx 10^5$, which is not our case, so from the spectra it will not be possible to distinguish τ_R from τ_d. However, since $g_1(t)/\sqrt{t}$ slope is negative, we do have reptation, and therefore the longest relaxation time is called τ_d.

In the non-linear flow regime the diffusion is not isotropic, and the diffusion tensor is defined as

$$g_{\alpha\beta}(t) = \langle [\mathbf{R}(t) - \mathbf{R}(0)] \cdot \mathbf{e}_\alpha [\mathbf{R}(t) - \mathbf{R}(0)] \cdot \mathbf{e}_\beta \rangle \tag{20}$$

For further data analysis, the advection of the center of mass $\mathbf{a}_0$ due to the bulk shear flow is subtracted from every point on the trajectory:

$$\mathbf{R}(t) \to \mathbf{R}(t) - \dot{\gamma} \Delta t \mathbf{e}_x \sum_{t'=-\infty}^{t} \mathbf{a}_0(t') \cdot \mathbf{e}_y \tag{21}$$

This allows to extract the diffusive component eliminating the macroscopic flow. The resulting diffusion tensor, divided by $\sqrt{t}$, is shown in Fig. 6. Straight lines indicate the expected slopes for Rouse, entanglement, and free diffusion (random jump).

The results can be summarized as follows:

- xx-direction (shear flow): The diffusion accelerates on all timescales, indicating disentanglement: $\tau_d \to \tau_e \approx$ const. The highest shear rate shows complete disentanglement and the diffusion becomes comparable to that of a single monomer, $N = 1$.

- yy-direction (shear gradient): The diffusion slows down at all timescales. The longest relaxation time is unchanged $\tau_d \approx \tau_d(\mathrm{Wi} = 0)$, while the onset of the entanglement time $\tau_e \to \tau$ decreases.

- zz-direction (vorticity): The entanglement time decreases $\tau_e \to \tau$, leading to slower

diffusion on the short time scales. Meanwhile, the disentanglement time τ_d becomes slightly shorter as well, resulting in an accelerated diffusion on long time scales.

- xy-direction (cross-correlated off-diagonal displacement): This component means that if the chain makes a random step along $+x$, it is also likely to make a random step along $+y$ axis. The magnitude of this correlation is 10^1-10^2 times weaker than the diagonal elements. The character of diffusion is that of a free random walk, although a Rouse-like and possibly slower character seems to emerge around τ_d for sufficiently high shear rates.

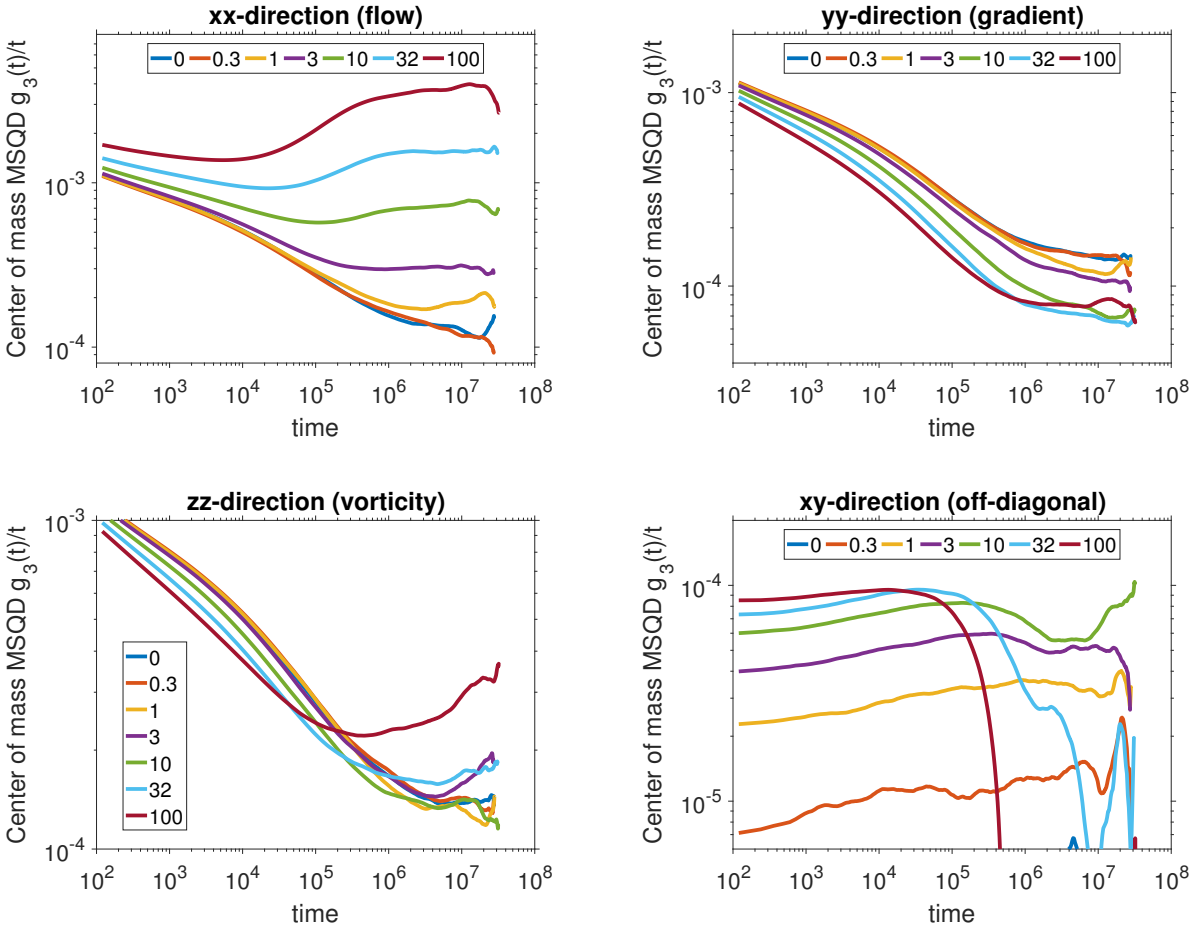

Figure 7: Center of mass diffusion spectrum. The legend indicates shear rate in Wi.

The central monomer diffusion is hard to access experimentally, so most measurements

are restricted to the center of mass diffusion:

$$g_3(t) = \langle [\mathbf{a}_0(t) - \mathbf{a}_0(0)]^2 \rangle \tag{22}$$

This quantity averages the contributions from all monomers, and the entanglement character becomes smeared. On the contrary, g_3 reflects the dynamics on large length scales. We plot the quantity $g_3(t)/t$ in Fig. 7, so that the long-time limit of each curve reaches a plateau corresponding to the self-diffusion coefficient. The overall trends seen in these plots are similar to Fig. 6: The diffusion speeds up along x, slows down along y on all time scales and slows down along z for short, but speeds up at longer time scales. However, without visible entanglements, the origins of the dynamical changes are obscured, unlike in Fig. 6 where the mechanisms of the non-linear flow are revealed more clearly.

Intermediate scattering function

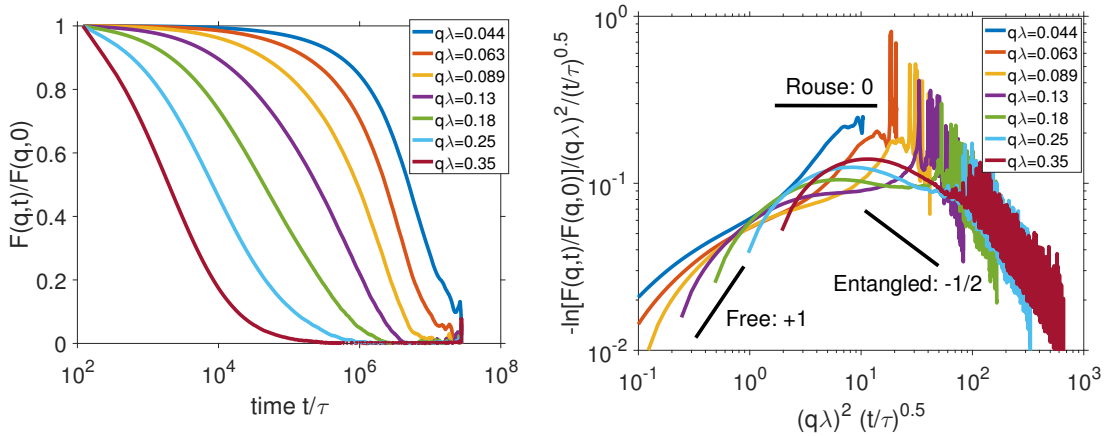

(a) Raw data

(b) Rescaled data

Figure 8: Intermediate scattering function at equilibrium. The same dataset is plotted in two different ways.

Yet another way to quantify diffusion is the intermediate scattering function. In the

simulation, at every step t we calculate the instantaneous form factor of every chain:

$$f_c(\mathbf{q},t) = \frac{1}{J}\sum_{j=1}^{J} e^{-i\mathbf{q}\cdot\mathbf{R}_{j,c}} \tag{23}$$

for a set of predetermined values of the wavevector $\mathbf{q}$, characteristic of a lengthscale $1/q$. The advection is subtracted in the same way as in Eq. (21). The cross-correlation of the form factor with its complex conjugate, averaged over all chains, is called the single chain coherent intermediate scattering function:

$$F(\mathbf{q},t) = \frac{1}{C}\sum_{c=1}^{C} \langle f_c(\mathbf{q},t) f_c(-\mathbf{q},0)\rangle \tag{24}$$

and is the quantity measured in neutron spin echo experiments. The simulation data in equilibrium is plotted in Fig. 8a. While analytical expressions are difficult and cumbersome to derive, certain key features of $F(q,t)$ are well known.[7] Particularly well studied is the Rouse model, which says that for the chain interior, $\lambda \ll 1/q \ll R_g$, during the corresponding time interval $1 \ll t/\tau \ll N^2$, all the q vectors collapse to a universal function $F(q,t) \approx e^{-q^2\sqrt{t}}$, or $-\ln(F) \approx q^2\sqrt{t}$. This latter quantity is plotted in Fig. (8b), normalized by $q^2\sqrt{t}$ to make the Rouse behaviour appear as a horizontal line.

The plot shows that at small $q < 1/R_g$, free diffusion is observed: $-\ln(F) \approx q^2 t$. Larger $q > 1/R_g$ vectors start probing the interior of the chain and Rouse dynamics emerges: $-\ln(F) \approx q^2\sqrt{t}$. At longer timescales, the slope turns negative approaching reptation: $-\ln(F) \approx q^2 t^{1/4}$. A stronger entanglement signature in $F(q,t)$ is visible for longer chains, which was recently reported for the quiescent situation.[54]

To extract changes under shear, we define the scattering excess:

$$\Delta F(\mathrm{Wi}) = F(q,t)/F(q,0) - F_0(q,t)/F_0(q,0) \tag{25}$$

which is the difference between the intermedite scattering function at rest and under shear.

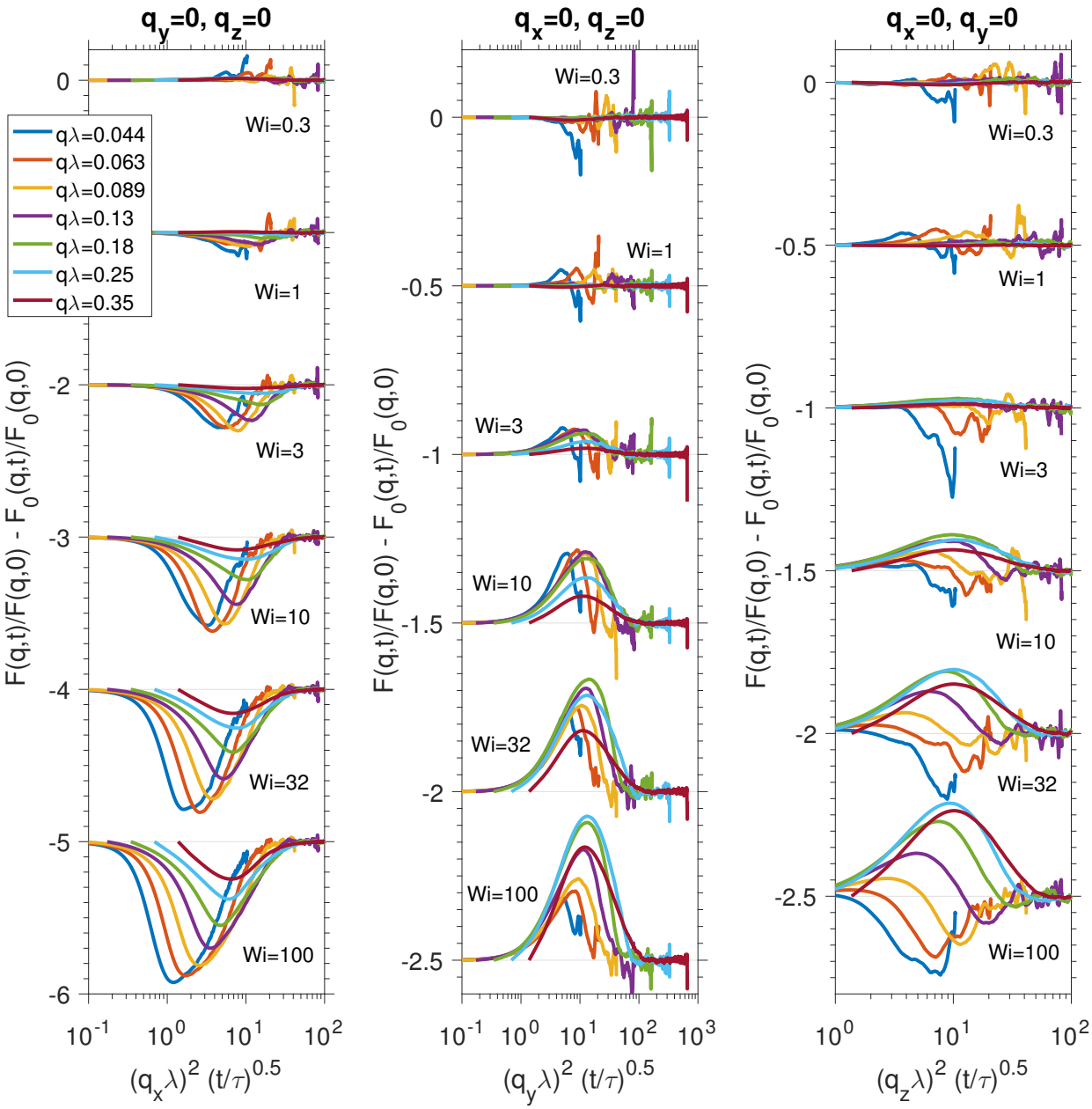

Figure 9: Intermediate scattering function excess ΔF. For clarity, data of different shear rates has been shifted by -1 in the first panel q_x, and by -0.5 in the other two panels.

The excess ΔF can range between $(-1, 1)$, where positive (negative) values indicate that there is a slowdown (speedup) of the dynamics. The simulation data for all shear rates and directions is shown in Fig. 9. Along the x direction the dynamics is accelerated for all q_x, while in the y direction the dynamics is slowed down for all q_y, although the amplitude of the effect is about three times weaker. The change is weakest along the z direction, but its behaviour is the most intricate. At short time scales, the dynamics is slowed down, but at longer time scales a speeding up is found. The q_z vectors corresponding to the interior of the chain (those which show a negative slope in Fig. 8b) display slowing down, while the very small $q_z < R_g$, corresponding to distances larger than the size of the chain, display speeding up.

Mechanical spectroscopy

A complementary approach to reveal polymer dynamics is to analyze the stress fluctuations. Specifically, the mechanical relaxation spectrum

$$G(t) = \frac{V}{k_B T} \langle \sigma_{xy}(t) \sigma_{xy}(0) \rangle \tag{26}$$

can be evaluated from equilibrium simulation data, as well as measured experimentally using small amplitude oscillatory shear. The Rouse model predicts that the stress should decay as $G \propto t^{-1/2}$, and reach zero at time $\tau_R \approx \tau N^2$. The reptation model, in contrast, suggests a plateau of height $G_0 \approx k_B T / \lambda^3 / N_e$ in stress, and eventually a decay at time $\tau_d \approx \tau (N/N_e)^{3.4}$.

The simulation gives access to six independent stress components: σ_{xy}, σ_{xz}, σ_{yz}, $N_1 = \sigma_{xx} - \sigma_{yy}$, $N_2 = \sigma_{yy} - \sigma_{zz}$, and $N_3 = \sigma_{xx} - \sigma_{zz}$. The third normal stress difference N_3 would usually be redundant since it can be expressed in terms of the N_1, N_2, and the pressure P which does not depend on shear rate. However, the pressure fluctuations are influenced by shear, and hence we keep the N_3.

The mean value of the steady state is subtracted from each signal, $\sigma_{\alpha\beta}(t) \to \sigma_{\alpha\beta}(t) - \langle \sigma_{\alpha\beta} \rangle$,

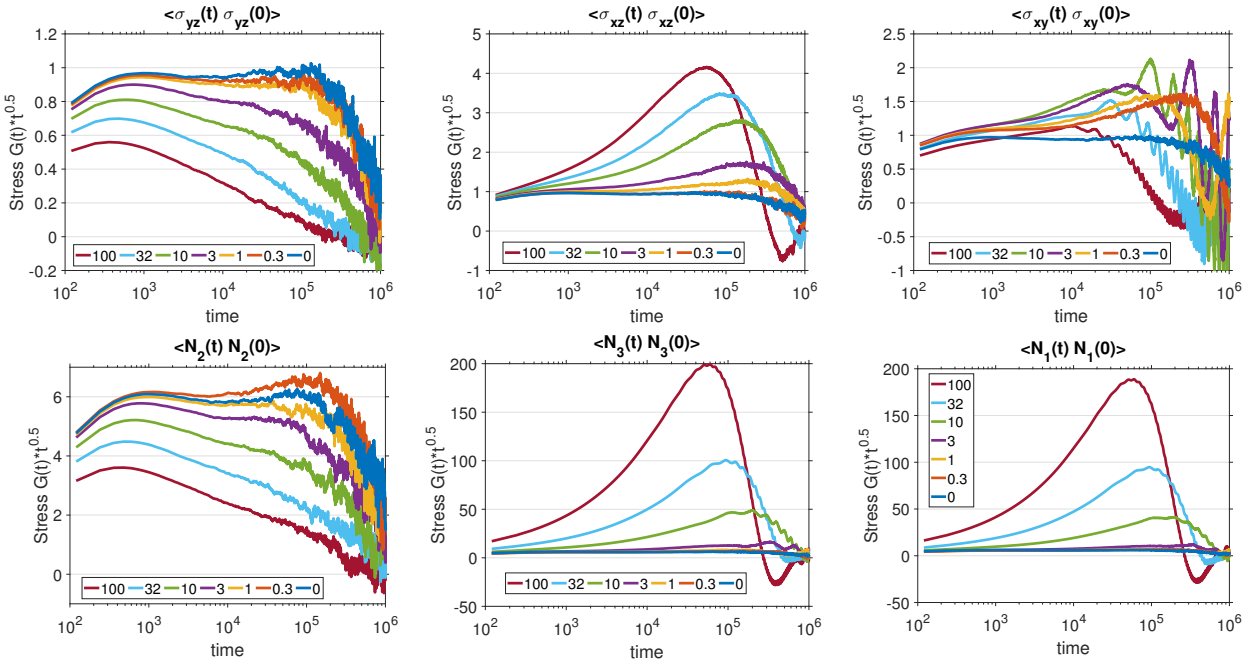

Figure 10: Stress autocorrelations

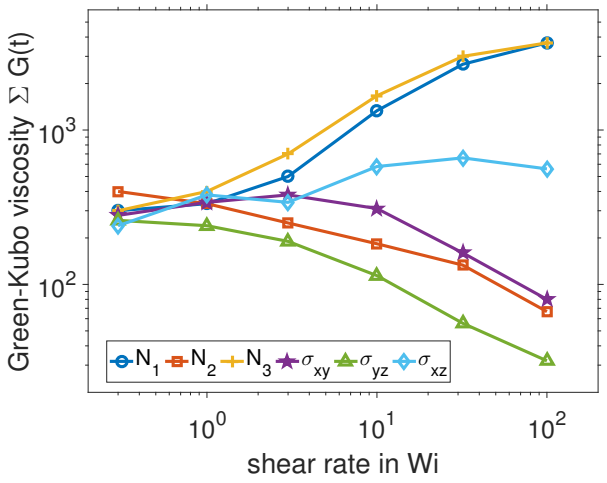

Figure 11: Green-Kubo viscosity

and all six autocorrelations are shown in Fig. 10. The data is rescaled to $G(t)\sqrt{t}$, so that the Rouse behaviour appears as a flat line, and a positive slope indicates the presence of entanglement dynamics. In equilibrium, the Green-Kubo formula can be used to obtain the zero-shear viscosity (see Eq. 4 in Ref.[7]):

$$\eta = \int_0^\infty dt\, G(t) \tag{27a}$$

$$= \int_0^\infty dt\, \frac{V}{5k_BT} \left[\langle\sigma_{xy}(t)\sigma_{xy}(0)\rangle + \langle\sigma_{yz}(t)\sigma_{yz}(0)\rangle + \langle\sigma_{xz}(t)\sigma_{xz}(0)\rangle\right] \tag{27b}$$

$$+ \frac{V}{30k_BT} \left[\langle N_1(t)N_1(0)\rangle + \langle N_2(t)N_2(0)\rangle + \langle N_3(t)N_3(0)\rangle\right] \tag{27c}$$

Far from equilibrium, the above formula may not have a straightforward interpretation, but the resulting values are nevertheless indicative of the fluctuations' amplitude multiplied by their duration, which is a useful quantity to compare among the different components as well as equilibrium. For a direct comparison, the shear stress contributions are divided by 5, the normal stress contributions are divided by 30, and all are plotted in Fig. 11. The results can be summarized as follows:

- x-axis (flow): The shear stress around this axis is σ_{yz}, and the normal stress difference $N_2 = \sigma_{yy} - \sigma_{zz}$, as geometrically illustrated in Fig. 14. Both shear and normal stress fluctuations decrease in amplitude $G(t = 0)$ as well as duration (τ_d smaller). The slope of $G(t)$ turns to negative indicating strong disentanglement in this direction.

- y-axis (gradient): The shear stress around this axis is σ_{xz}, and the normal stress difference $N_3 = \sigma_{xx} - \sigma_{zz}$. The amplitude of fluctuations $G(t = 0)$ stays roughly the same, and the relaxation time τ_d is hardly affected by shear. However, there is a very strong change of character, with a clear entanglement peak emerging for both shear and normal stress. Based on the Green-Kubo formula one could say that there is a strong increase in "viscosity". The positive slope starts early on, so the mechanism seems to be that the entanglement onset time decreases: $\tau_e \to \tau$.

- z-axis (vorticity). The shear stress around this axis is σ_{xy}, and the normal stress difference $N_1 = \sigma_{xx} - \sigma_{yy}$. Unfortunately, the shear stress data is contaminated by a parasitic numerical effect due to finite pixel size used to evaluate the excluded volume force. The oblique pixel shape induces numerical stress, which oscillates at precisely the same frequency as the imposed shear, $f = \dot{\gamma}$. The use of a conjugate grid (Eq. (46)) helps, but is not sufficient to remove the bias completely. For now let us ignore the unphysical oscillating component and discuss trends. The shear stress fluctuations change very little compared to the two other axes. There seems to be a small decrease in onset time τ_e, leading to some entanglement character emerging, but the relaxation time τ_d also decreases slightly. The major difference becomes apparent when we look at the normal stress N_1, which shows strong entanglement similar to N_3, but is not accompanied by a comparable change of shear stress, unlike σ_{xz}. In terms of the Green-Kubo formula, the shear contribution to "viscosity" decreases slightly, while the normal contribution increases very strongly.

Overall, our results show a strong decrease of stress fluctuations associated with the x (flow) axis, and a strong increase of fluctuations around the y (gradient) axis. The data in the z (vorticity) axis is influenced by the numerical approximations required to have fast computation, but the crude result is that the shear stress fluctuations decrease slightly, while the normal stress fluctuations increase strongly.

In the non-linear flow regime the various stress components are not independent, unlike in equilibrium. In fact, there are six non-zero cross-correlations, shown in Fig. 12. While the mean pressure does not depend on shear rate, its fluctuations increase, leading to an increase in the cross-correlations $\langle N_1(t)P(0)\rangle$ and $\langle P(t)\sigma_{xy}(0)\rangle$. In the simulation we have fixed the density, which leads to pressure fluctuations, but in a rheological experiment it is more common to have a fixed pressure, which would then result in density fluctuations of the bulk (not to be confused with local density fluctuations which are always present and give rise to the liquid structure factor, discussed in Appendix B). The intriguing panels are the cross-

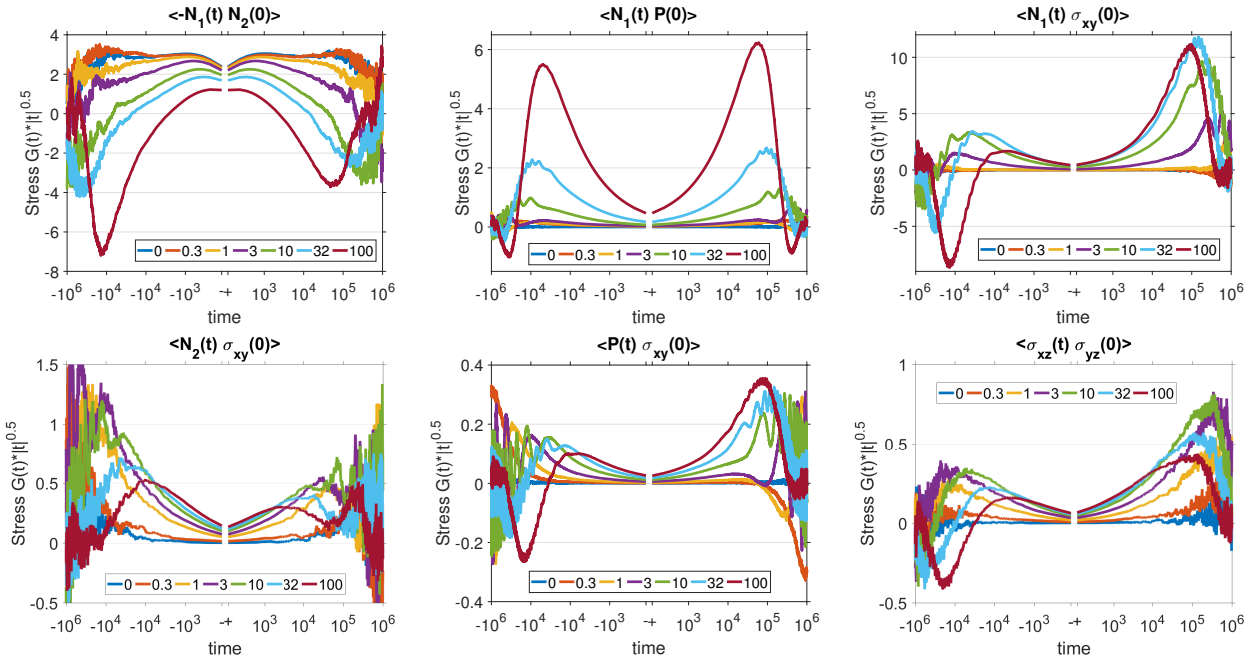

Figure 12: Stress crosscorrelations

correlations $\langle N_1(t)\sigma_{xy}(0)\rangle$ and $\langle\sigma_{xz}(t)\sigma_{yz}(0)\rangle$. Both of them have quite a similar spectrum, which is symmetric for short timescales (indicating thermal equilibrium), but switching to an antisymmetric one for long timescales (suggesting an irreversible process and possibly a causal relationship).

Discussion

Steady-state structure

In Fig. 13 we plot the inertia tensor components x and z, defined in Eq. (15), normalized to equilibrium. There is a good agreement between our soft blobs, the hard beads, and the phenomenological slip-links model. The agreement with the available experimental data is more qualitative. Due to the possibility of labeling and its intrinsic nature to directly measure pair correlation distributions SANS is the only tool to investigate the single chain form factor of a polymer melt,[51] and we now review the literature data.

Some examples of low glass transition and low viscosity polymers, which are easier to

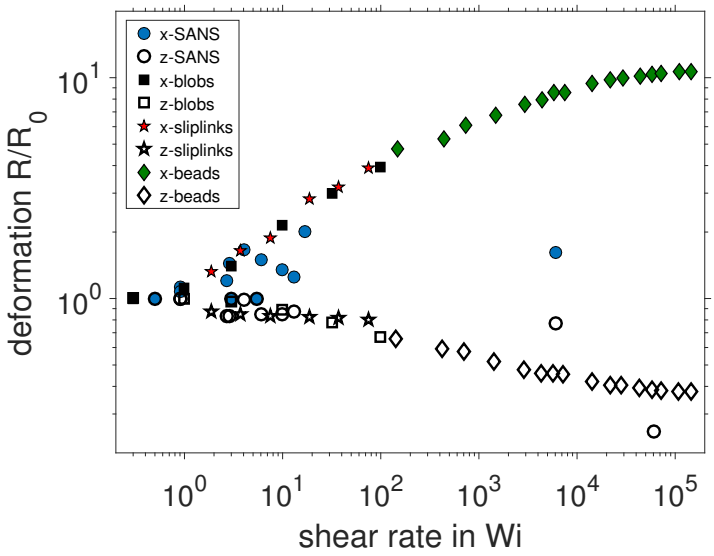

Figure 13: Radius of gyration along flow $\sqrt{3R_{xx}^2/R_g^2}$ and vorticity $\sqrt{3R_{zz}^2/R_g^2}$ directions: rheo-SANS experiments, blob simulations (this work), slip-links simulations,[55] and KG simulations (beads)[46]

shear in Couette flow are polydimethylsiloxane (PDMS) and polybutadien (PBD). *In situ* steady flow SANS experiments have been done on both not showing any measurable asymmetry of the single chain form factor. The highest shear rate for the PBD experiment[56] in Couette geometry was $\mathrm{Wi} = 5.4$ and for the PDMS experiment[37] in cone/plate geometry was $\mathrm{Wi} = 3$. In both cases the shear rate normalized to the Rouse time τ_R was $\mathrm{Wi} \cdot N_e/N = 0.2$. The only Couette flow *in situ* shear experiment that showed anisotropy was performed in a Couette cell with polystyrene (PS) at $\mathrm{Wi} \approx 1$ or $\mathrm{Wi} \cdot N_e/N \approx 0.1$, however the relaxation time was not measured, so the exact Weissenberg number is questionable.[25]

An *in situ* slit shear SANS experiment was done with PS[26] at 170 °C. Here local flow rates of $\mathrm{Wi} = 13$ were reached with $\mathrm{Wi} \cdot N_e/N = 1$. An asymmetry of the radii of gyration parallel and perpendicular to flow of up to 1.44 was detected. A retake of this experiment at a higher temperature yielded even higher asymmetries of up to 1.7 although the dimensionless shear rates were considerably lower.[27,28] All of these shear rates correspond, however, to the centreline extensional shear rate. The shear rate at the wall is about 5.5 times higher.

Ex situ shear SANS has been performed on PS[29] where the maximum shear rate at quenching is estimated to be $\mathrm{Wi} = 4$ or $\mathrm{Wi} \cdot N_e/N = 0.8$ and an asymmetry of 1.7 was found between the radii of gyration in flow and vorticity directions. The exact Weissenberg number is difficult to estimate due to the rise of the relaxation time during quenching.

An *ex situ* elongational flow experiment was reported recently using PS[32] reaching shear rates of $\mathrm{Wi} = 17$ or $\mathrm{Wi} \cdot N_e/N = 2$. Here a stretch of 2 was reported for the single chain form along the flow.

A series of *ex situ* very fast elongational flow studies have probed extensional flow rates much faster than the inverse Rouse time $1/\tau_R$. For polyisoprene (PI) at $\mathrm{Wi} \approx 6000$ or $\mathrm{Wi} \cdot N_e/N = 120$ the authors report swelling ratios of the radii of gyration of 1.62 in the flow direction and 0.77 in the vorticity direction.[30] Other *ex situ* studies on PS report R_g shrinking down to 0.25 along vorticity.[31] In these studies, however the sample is quenched after stopping flow, so there is some time for the chain to relax, although generally this time is orders of magnitude shorter than the Rouse time.

In summary, it is evident that the single chain form factor of linear polymers stretches along the shear flow, accompanied by a smaller collapse perpendicular to it. However, an open experimental question remains as to whether this effect becomes apparent at $\mathrm{Wi} \approx 1$ or at higher rates $\mathrm{Wi} \approx N/N_e$. Moreover, no stretching ratios higher than 2 were reported up to now. In contrast, the consensus among various simulations is that the structural change starts at $\mathrm{Wi} \approx 1$, coinciding with the onset of non-linear rheology. A possible explanation is that both the inertia, Eq. (15), and the stress, Eq. (16), tensors have quite similar microscopic definitions, so a change of one must be accompanied by a change of the other, in the same direction but by a different magnitude.

Dynamical structure

The physics that has emerged from our simulation is summarized in Fig. 14. The biggest effect is seen along the flow direction, x, where chains are strongly elongated, and both

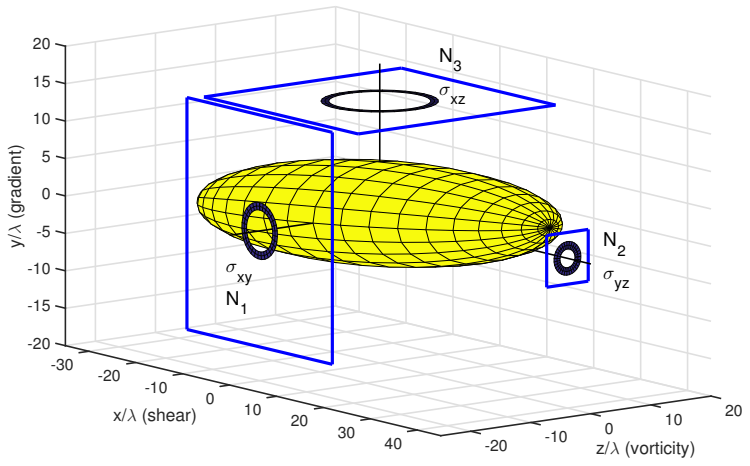

Figure 14: Summary of polymer dynamics at Wi = 32. The inertia ellipsoid is plotted at the center. The area of circles (squares) around each axis corresponds to the Green-Kubo integral of the shear (normal) stress fluctuations, in arbitrary units.

shear and normal stress fluctuations around this axis are suppressed. This is accompanied by faster diffusion at all scales. One could loosely apply the Einstein-Stokes equation

$$D = \frac{k_B T}{6\pi\eta R} \tag{28}$$

to relate the diminished stress fluctuations (or the "viscosity" $\eta = \int G(t)\,dt$), with a higher chain diffusivity D. An opposite and weaker trend is observed along the gradient direction, y. The chain size shrinks, while both shear and normal stress fluctuations increase around this axis, which is accompanied by slower diffusion at all scales.

The weakest effects are found in the vorticity direction, z. The chain size decreases by a small amount. The stress fluctuations are ambivalent, with the shear stress contribution decreasing slightly, while the normal stress contribution is increased by a much larger amount. The corresponding change of diffusion is ambivalent too, decreasing on short timescales, but eventually catching up and reaching a net speedup at long timescales.

Recent experimental studies on sheared polymers have brought focus on the dynamical fluctuations. Particularly relevant are *in situ* neutron spin echo experiments under shear,[57]

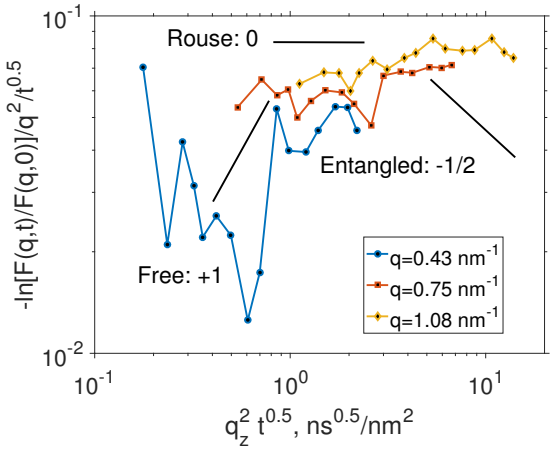

(a) Analysis of the static measurement, comparable to Fig. 8b

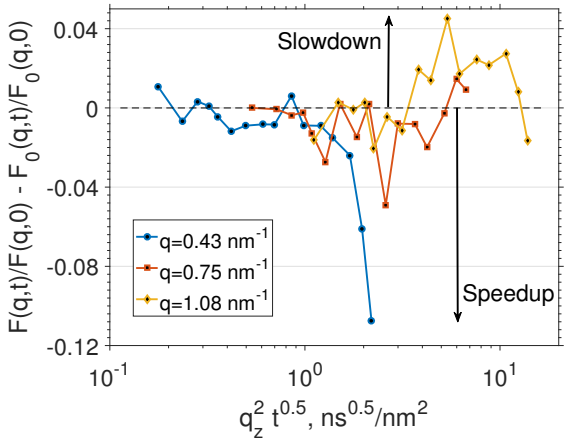

(b) Scattering excess under shear, comparable to Fig. 9

Figure 15: Rheo - neutron spin echo results for PDMS melt of $M_w = 1.9 \times 10^5\,\mathrm{g\,mol^{-1}}$, sheared at $\dot{\gamma} = 100\,\mathrm{s^{-1}}$. Original data taken from Ref.[37]

which measure the intermediate scattering function $F(q_z, t)$ along the z (vorticity) axis. The data extracted from Ref.[37] is represented in Fig. 15, which shows a change in the scattering at a shear rate of about $\mathrm{Wi} = \dot{\gamma}\tau_d = 1.4$. There is a visible speedup of dynamics at the smallest q vector, which can be compared with a similar trend seen in the simulated data, Fig. 9. The highest q vector shows a slight slowdown, although it is within the error bars and further experiments are needed to verify this effect.

Dielectric spectroscopy under shear measures the dynamics of the end-to-end vector $\mathbf{R}_1 - \mathbf{R}_J$. Data on entangled polyisoprene solutions in the shear gradient direction y shows a clear slowdown for star polymers and a very slight slowdown for linear polymers.[36] Although we have not analyzed the end-to-end vector, the trend of overall slowdown along y agrees well with the simulation. Also worth mentioning is a neutron quasielastic scattering study on sheared P85 triblock copolymer micelles,[58] reporting a slowdown of diffusion in the y direction. A contradiction was found in an earlier simulation based on slip-links.[55] Their conclusion is that the diffusion speeds up along all three directions, and moreover, both y and z axes show the exact same speedup.

Superposition rheology can probe shear stress dynamics perpendicular, σ_{yz}, and parallel,

σ_{xy}, to the flow axis x. Measurements on entangled polyisobutene solutions[35] and more recently wormlike micelles[59] both report a strong speedup of the two σ_{yz} and σ_{xy} components, although the analysis of the latter is complicated and the result is not as reliable as in the perpendicular case. These results agree with the findings of our simulations in a qualitative way.

Summary and perspectives

In this article we have simulated the dynamics of long, $N/N_e = 8.5$, linear monodisperse chains under a steady shear flow. The source code is provided, and can be straightforwardly extended to include polydispersity, different chain architectures (ring, comb, brush), and non-steady shear (oscillatory, step).

Our code generates information on the physics of entangled multi chain systems far from equilibrium. The model is kept simple not considering any short range chemical interactions, but focusing on the general phenomena of the chain motion on the scale significantly larger than the monomer size λ. Entangled polymers are notoriously time consuming to simulate. We overcame this limitation by applying the approximate convolution theorem, Eq. (12b). Mathematical efforts are underway to provide more isotropic discretization schemes without sacrificing speed[60] and our code may benefit from such developments in the future.

We have analyzed the relaxation spectra from both structural and mechanical points of view. The most intriguing changes are along the vorticity direction. At the moment we are not aware of theoretical explanations of our findings. However, it is clear that the study of dynamical fluctuations provides a much more detailed picture than just the steady-state values alone (e.g. viscosity or radius of gyration vs shear rate).

Author contributions

A.K. performed the simulations and data analysis. P.G. and M.W. have discussed the neutron scattering experiments. The manuscript was written by A.K. with contributions of all authors.

Acknowledgements

The authors thank Jean-Louis Barrat for his valuable advice. Gunnar K. Palsson, Anton Devishvili, and Franz A. Adlmann have contributed to the development of the simulation software. The Carl-Tryggers stiftelse as well as the Swedish research council are acknowledged for financial support.

Appendix A. Oblique coordinate system

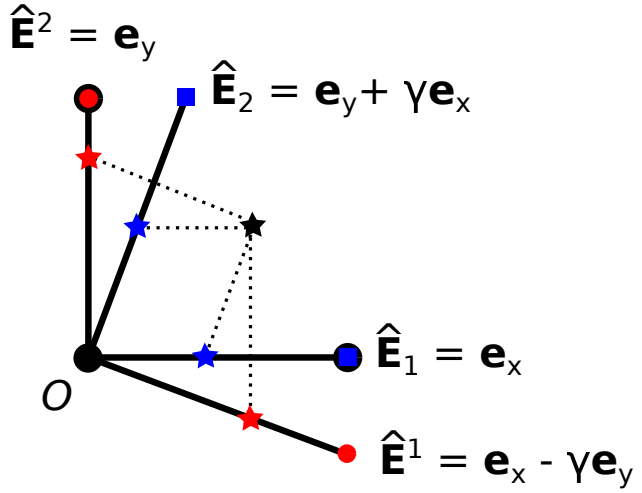

Figure 16: The definition of an oblique coordinate system of some arbitrary strain $\gamma = 0.375$ in terms of the rectangular basis $(\mathbf{e}_x, \mathbf{e}_y)$. The oblique system has two bases, the covariant $(\hat{\mathbf{E}}_1, \hat{\mathbf{E}}_2)$ and the contravariant $(\hat{\mathbf{E}}^1, \hat{\mathbf{E}}^2)$. A particle position $\mathbf{r}$ shown by a black star is decomposed into its covariant and contravariant components.

We closely follow the results originally derived in Ref.[61] The key message is that the oblique coordinate system is non-orthogonal, and therefore special care must be taken to

distinguish between covariant vectors such as particle positions $\mathbf{r}$, and contravariant vectors such as forces $\mathbf{f}$ or wavevectors $\mathbf{q}$.

A particle position in the rectangular coordinate system $(\mathbf{e}_x, \mathbf{e}_y, \mathbf{e}_z)$ can be decomposed into its Cartesian components (x, y, z):

$$\mathbf{r} = x\mathbf{e}_x + y\mathbf{e}_y + z\mathbf{e}_z. \tag{29}$$

In terms of the rectangular unit vectors, the oblique coordinate system of strain γ is defined by the covariant basis:

$$\hat{\mathbf{E}}_1 = \mathbf{e}_x \tag{30a}$$

$$\hat{\mathbf{E}}_2 = \gamma\mathbf{e}_x + \mathbf{e}_y \tag{30b}$$

$$\hat{\mathbf{E}}_3 = \mathbf{e}_z \tag{30c}$$

In other words, the metric tensor of the oblique system is given by

$$g_{ij} = \hat{\mathbf{E}}_i \cdot \hat{\mathbf{E}}_j = \begin{pmatrix} 1 & \gamma & 0 \\ \gamma & 1+\gamma^2 & 0 \\ 0 & 0 & 1 \end{pmatrix} \tag{31}$$

As illustrated in Fig. 16, the position of a particle in the oblique system, denoted by $\hat{\mathbf{r}}$, is expressed as

$$\hat{\mathbf{r}} = \hat{x}^1\hat{\mathbf{E}}_1 + \hat{x}^2\hat{\mathbf{E}}_2 + \hat{x}^3\hat{\mathbf{E}}_3 \tag{32}$$

where its coordinate components in the oblique system can be found by solving the equation

$\hat{\mathbf{r}} = \mathbf{r}$:

$$\hat{x}^1 = x - \gamma y \tag{33a}$$

$$\hat{x}^2 = y \tag{33b}$$

$$\hat{x}^3 = z \tag{33c}$$

The simulated polymer network is periodic in these coordinates. The inverse is

$$x = \hat{x}^1 + \gamma \hat{x}^2 \tag{34a}$$

$$y = \hat{x}^2 \tag{34b}$$

$$z = \hat{x}^3 \tag{34c}$$

The interaction potential is a scalar quantity, in our case a Gaussian:

$$U(\mathbf{r}) = \exp\left[-\frac{\mathbf{r}^2}{2\lambda^2}\right] = \exp\left[-\frac{(x^2+y^2+z^2)}{2\lambda^2}\right]. \tag{35}$$

A scalar remains invariant regardless of a coordinate system, so to express it in the oblique coordinates, we simply plug in the values from Eq. (34):

$$\hat{U}(\hat{\mathbf{r}}) = \exp\left[-\frac{(\hat{x}^1+\gamma\hat{x}^2)^2 + (\hat{x}^2)^2 + (\hat{x}^3)^2}{2\lambda^2}\right] \tag{36}$$

The force, in the oblique system, is given by the gradient:

$$\hat{\mathbf{f}}(\hat{\mathbf{r}}) = -\hat{\nabla}\hat{U}(\mathbf{r}) = -\left[\hat{\mathbf{E}}^1\frac{\partial\hat{U}}{\partial\hat{x}^1} + \hat{\mathbf{E}}^2\frac{\partial\hat{U}}{\partial\hat{x}^2} + \hat{\mathbf{E}}^3\frac{\partial\hat{U}}{\partial\hat{x}^3}\right] \tag{37}$$

which is expanded in terms of the contravariant basis vectors:

$$\hat{\mathbf{E}}^1 = \mathbf{e}_x - \gamma \mathbf{e}_y \tag{38a}$$

$$\hat{\mathbf{E}}^2 = \mathbf{e}_y \tag{38b}$$

$$\hat{\mathbf{E}}^3 = \mathbf{e}_z \tag{38c}$$

These are defined to be conjugate to the covariant basis vectors: $\hat{\mathbf{E}}_i \cdot \hat{\mathbf{E}}^j = \delta_i^j$, and in particular $\hat{\mathbf{E}}_2 \cdot \hat{\mathbf{E}}^1 = (\gamma \mathbf{e}_x + \mathbf{e}_y) \cdot (\mathbf{e}_x - \gamma \mathbf{e}_y) = 0$. Morevover, the contravariant metric tensor

$$g^{ij} = \hat{\mathbf{E}}^i \cdot \hat{\mathbf{E}}^j = \begin{pmatrix} 1+\gamma^2 & -\gamma & 0 \\ -\gamma & 1 & 0 \\ 0 & 0 & 1 \end{pmatrix} \tag{39}$$

is clearly the inverse of the covariant one: $g_{ij} g^{ij} = 1$. Let us be very clear on what are the specific components of the force, in terms of the oblique contravariant basis:

$$\hat{f}_1 = -\frac{\partial \hat{U}}{\partial \hat{x}^1} = \left(\frac{\hat{x}^1 + \gamma \hat{x}^2}{\lambda^2} \right) \hat{U}(\hat{\mathbf{r}}) \tag{40a}$$

$$\hat{f}_2 = -\frac{\partial \hat{U}}{\partial \hat{x}^2} = \left(\frac{\gamma \hat{x}^1 + (1+\gamma^2)\, \hat{x}^2}{\lambda^2} \right) \hat{U}(\hat{\mathbf{r}}) \tag{40b}$$

$$\hat{f}_3 = -\frac{\partial \hat{U}}{\partial \hat{x}^3} = \left(\frac{\hat{x}^3}{\lambda^2} \right) \hat{U}(\hat{\mathbf{r}}) \tag{40c}$$

Just like the position vector, the force vector can be expanded in either the rectangular or the oblique systems:

$$\mathbf{f} = f_x \mathbf{e}_x + f_y \mathbf{e}_y + f_z \mathbf{e}_z \tag{41a}$$

$$= \hat{f}_1 \hat{\mathbf{E}}^1 + \hat{f}_2 \hat{\mathbf{E}}^2 + \hat{f}_3 \hat{\mathbf{E}}^3 \tag{41b}$$

which leads to its rectangular components

$$f_x = \hat{f}_1 \tag{42a}$$

$$f_y = \hat{f}_2 - \gamma \hat{f}_1 \tag{42b}$$

$$f_z = \hat{f}_3 \tag{42c}$$

Having presented all the necessary formulas, we now outline the algorithm required to evaluate the excluded volume force in the oblique periodic system.

1. We start off with a set of all particle positions (x, y, z) given in the usual rectangular coordinates. A fixed strain value γ is given as well.

2. The positions are transformed into the oblique system: $(x, y, z) \to (x - \gamma y, y, z)$, and the periodic boundary conditions are applied: $\hat{\mathbf{r}} = \hat{\mathbf{r}} - L\,\texttt{floor}\,(\hat{\mathbf{r}}/L)$. We are now folded inside the central oblique box, which is periodic along its covariant unit vectors.

3. A density histogram $\hat{\rho}(\hat{\mathbf{r}})$ is constructed, which holds the number of particles in every oblique pixel $\hat{\mathbf{r}} = L\left(k_1\hat{\mathbf{E}}^1 + k_2\hat{\mathbf{E}}^2 + k_3\hat{\mathbf{E}}^3\right)$ where the indices run from $k = 1,\, 2,\, \ldots, K = \texttt{round}(L/\Delta x)$, and Δx is the pixel width.

4. The density is Fourier-transformed into the oblique reciprocal space:

$$\hat{\rho}(\hat{\mathbf{q}}) = \sum_{\hat{\mathbf{r}}} \hat{\rho}(\hat{\mathbf{r}}) e^{-i\hat{\mathbf{r}}\cdot\hat{\mathbf{q}}} \tag{43}$$

   Notice that the components of the reciprocal lattice vector $\hat{\mathbf{q}} = (\hat{q}_1, \hat{q}_2, \hat{q}_3)$ come out in the contravariant basis defined in Eq. (38), because this basis has the unique property that

$$\hat{\mathbf{r}}\cdot\hat{\mathbf{q}} = \left(\hat{x}^1\hat{\mathbf{E}}_1 + \hat{x}^2\hat{\mathbf{E}}_2 + \hat{x}^3\hat{\mathbf{E}}_3\right)\cdot\left(\hat{q}_1\hat{\mathbf{E}}^1 + \hat{q}_2\hat{\mathbf{E}}^2 + \hat{q}_3\hat{\mathbf{E}}^3\right) = \hat{x}^1\hat{q}_1 + \hat{x}^2\hat{q}_2 + \hat{x}^3\hat{q}_3 \tag{44}$$

5. Steps 3-4 are repeated for the force kernel. First, the force array $\hat{\mathbf{f}}(\hat{\mathbf{r}})$ is declared in the real oblique space, and then it is Fourier-transformed to the reciprocal oblique space to give $\hat{\mathbf{f}}(\hat{\mathbf{q}})$.

6. The force on every oblique pixel $\hat{\mathbf{r}}$ is found by the convolution theorem:

$$\hat{\mathbf{F}}(\hat{\mathbf{r}}) = \texttt{IFFT}[\hat{\rho}(\hat{\mathbf{q}}) \cdot \hat{\mathbf{f}}(\hat{\mathbf{q}})] \tag{45}$$

7. Lastly, the oblique force is transformed to the rectangular system (the inverse of step 2, but for the contravariant basis): $(\hat{F}_1, \hat{F}_2, \hat{F}_3) \to (\hat{F}_1, \hat{F}_2 - \gamma\hat{F}_1, \hat{F}_3) = (F_x, F_y, F_z)$. These force components are then used in the equation of motion, Eq. (7), solved in the rectangular system as usual.

The strain position is updated at every time step, $\gamma \to \gamma + \dot{\gamma}\Delta t$, and folded as close as possible to the origin: $\gamma \to \gamma - \texttt{round}(\gamma)$. In addition, it must be noted that the use of the discrete convolution introduces some numerical anisotropy due to the finite size of the pixels. In equilibrium, the pixels are rectangular, and the numerical anisotropy is symmetric around every axis, which does not result in a net bias. When the pixels are oblique, however, the anisotropy tilts and produces a net numerical stress, which is unphysical and is not related to the shear flow. In fact, the numerical stress would persist even at equilibrium, if we would choose to simulate a system in a fixed oblique periodic system of $\gamma \neq 0$. To mitigate this parasitic effect, we keep track of the total accumulated strain

$$\gamma_{\text{sum}} = \sum \gamma(t) \tag{46}$$

and for every new timestep we choose the image of γ which would bring the accumulated strain γ_{sum} as close to zero as possible. For instance, in the example of Fig. 2, the strain is $\gamma = 0.232$, but one could equally well describe the system using a strain $\gamma^* = \gamma - 1 = -0.768$. Therefore, our code propagates two timesteps using the value γ, and the third step would

use the conjugate γ^*, because $|3\gamma - 1| < |3\gamma|$.

Appendix B. Detailed fluid structure

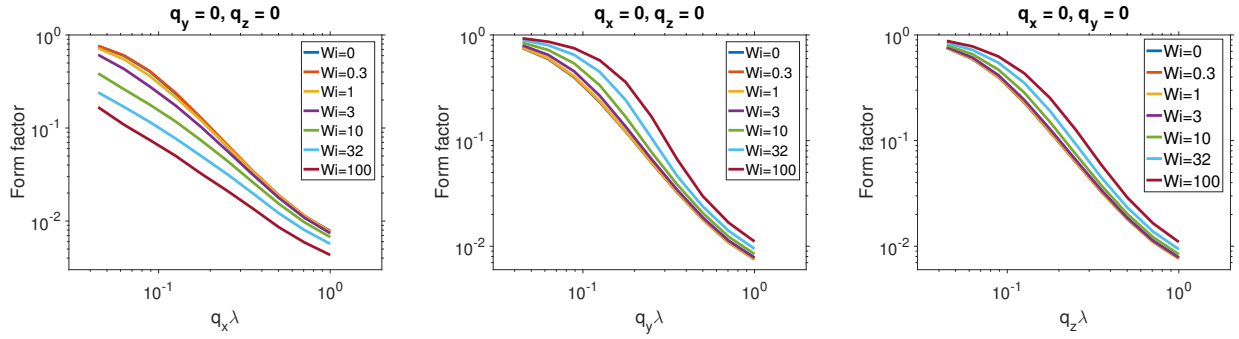

Figure 17: Single chain form factor

Experimentally, the radius of gyration can be studied by SANS, which measures the single chain form factor, microscopically defined as

$$F(\mathbf{q}) = \frac{1}{C}\sum_{c=1}^{C}\left|\frac{1}{J}\sum_{j=1}^{J} e^{-i\mathbf{q}\cdot\mathbf{R}_{c,j}}\right|^2 . \tag{47}$$

For very small wavevectors q one can show that the form factor is directly related to the radius of gyration, $F(q) \approx e^{-q^2 R_g^2}$, while for larger q the scattered signal contains additional information from the internal structure of the chains. The simulated form factor is plotted in Fig. 17 for a series of q vectors chosen along each coordinate axis. The information here is similar to the radius of gyration plot, Fig. 3, namely the chain stretches along x, but shrinks along y and z axes. The definition of the form factor, Eq. (47), is such that $F(\mathbf{q} = 0) = 1$, but in the x direction we see a drop of intensity for small q. This is expected for a strongly stretched polymer, whose Fourier transform approaches a Dirac delta peak at ultra small q, which we did not consider, since it starts to exceed the size of the simulation box and takes a very long time to relax (see the intermediate scattering function in Fig. 8).

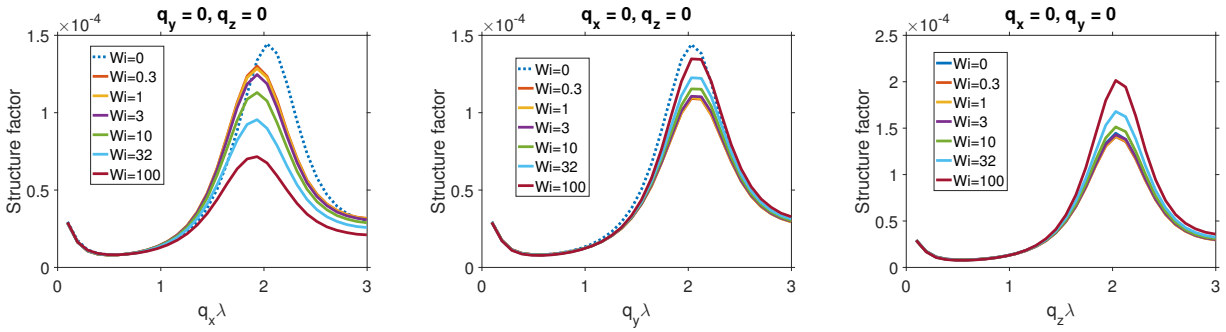

Figure 18: Liquid structure factor

The structure factor is defined as follows:

$$S(\mathbf{q}) = \left| \frac{1}{CJ} \sum_{c=1}^{C} \sum_{j=1}^{J} e^{-i\mathbf{q}\cdot\mathbf{R}_{c,j}} \right|^2 \tag{48}$$

Some radial cuts are plotted in Fig. 18, and 2D cuts are plotted in Fig. 21. At small q the structure is not affected by shear which is related to the fact that the pressure is constant. At high q we have one liquid peak which corresponds to the distance between two neighbouring blobs. The position and width of this peak do not change under shear. The intensity decreases along x-axis, meaning that the ordering is more random (i.e. more gas-like), and the opposite is seen along y and z axes, although the magnitude of change is smaller. The overall intensity of the structure factor is much lower than the form factor. In fact, for a perfectly uniform system, the structure factor would be a Kronecker delta peak: $S(\mathbf{q} = 0) = 1$ and zero for all other pixels. If there are small density fluctuations, then $S(\mathbf{q} > 0)$ increases slightly above zero, which is what we observe.

Although not studied experimentally, we found it useful to investigate the structure factor of the centers of mass alone:

$$S_0(\mathbf{q}) = \left| \frac{1}{C} \sum_{c=1}^{C} e^{-i\mathbf{q}\cdot\sum_j \mathbf{R}_{c,j}/J} \right|^2 \tag{49}$$

This function is plotted in Fig. 19 (radial cuts) and Fig. 22 (2D cuts), and tells us how the chains are arranged with respect to one another. Under shear, the ordering becomes

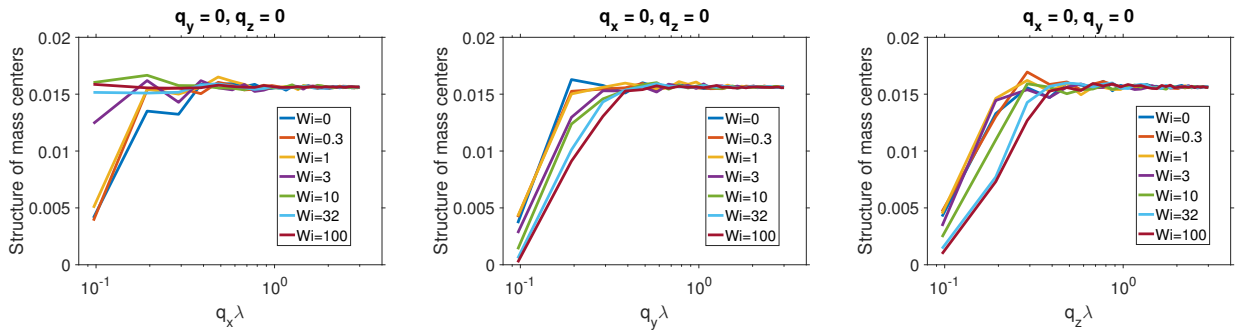

Figure 19: Structure of chain centers of mass

structureless (ideal gas) along the x-axis, while more ordering appears along y and z. These scattering patterns quantify the picture seen in Fig. 5.

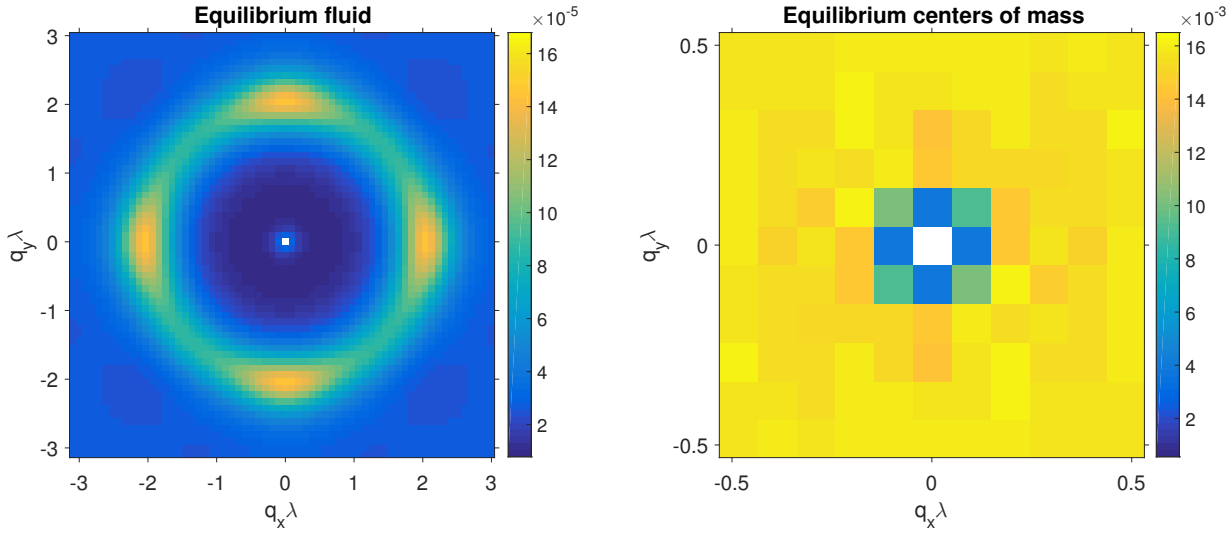

Figure 20: Cross-sections of the scattering function at equilibrium

Fig. 20 shows the 2D cross sections of the liquid structure factor and the centers of mass structure factor at equilibrium. At high q we can see four-fold anisotropy, which is a numerical artifact due to the finite pixel size, as discussed in the main text. The same quantities under shear Wi = 32 are shown in Figs. 21 and 22 respectively, for the three different axes.

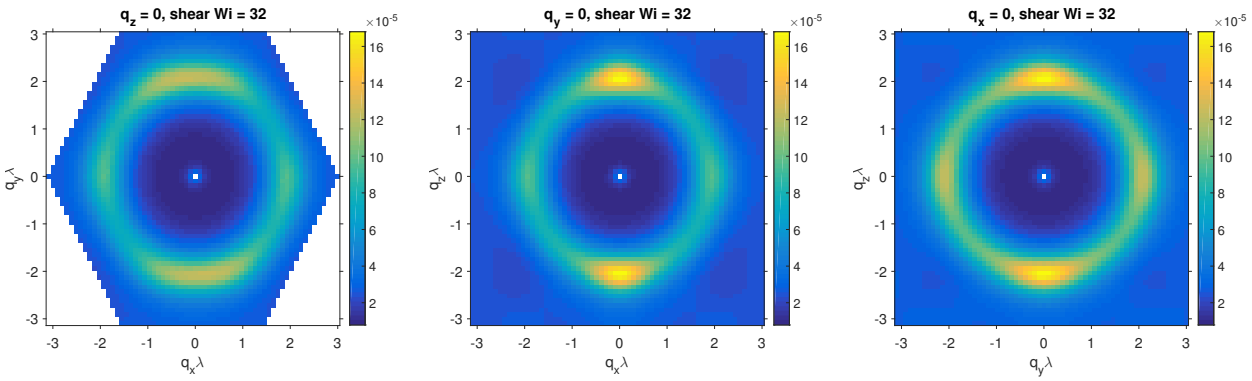

Figure 21: Cross-sections of the scattering function under shear Wi = 32

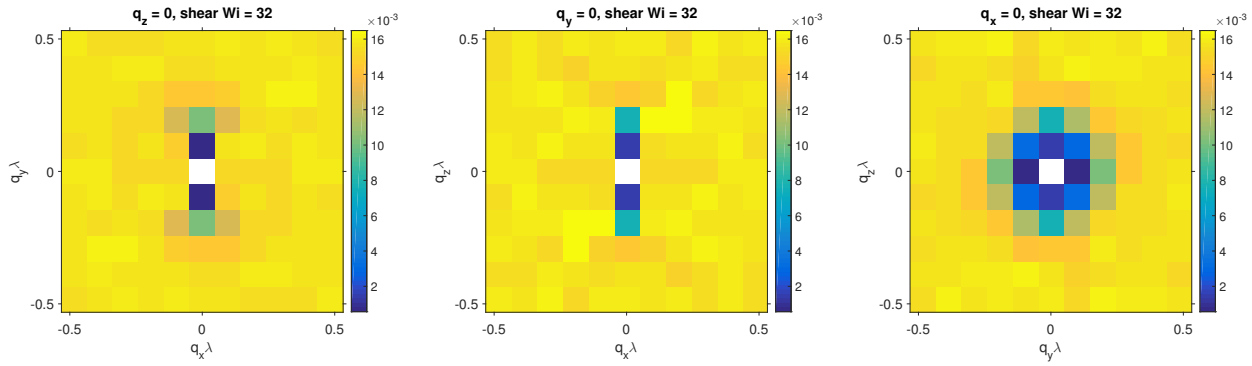

Figure 22: Cross-sections of the centers of mass scattering pattern under shear Wi = 32

References

(1) Cavaille, J.; Jourdan, C.; Perez, J.; Monnerie, L.; Johari, G. Time-temperature superposition and dynamic mechanical behavior of atactic polystyrene. *Journal of Polymer Science Part B: Polymer Physics* **1987**, *25*, 1235–1251.

(2) Kasaai, M. R.; Charlet, G.; Arul, J. Master curve for concentration dependence of semidilute solution viscosity of chitosan homologues: the Martin equation. *Food Research International* **2000**, *33*, 63–67.

(3) Wingstrand, S. L.; Alvarez, N. J.; Huang, Q.; Hassager, O. Linear and nonlinear universality in the rheology of polymer melts and solutions. *Physical review letters* **2015**, *115*, 078302.

(4) Cho, K. S.; Ahn, K. H.; Lee, S. J. Universality of linear viscoelasticity of monodisperse linear polymers. *Journal of Polymer Science Part B: Polymer Physics* **2004**, *42*, 2730–2737.

(5) de Gennes, P.-G. Reptation of a polymer chain in the presence of fixed obstacles. *The journal of chemical physics* **1971**, *55*, 572–579.

(6) Doi, M.; Edwards, S. F. *The theory of polymer dynamics*; oxford university press, 1988; Vol. 73.

(7) Likhtman, A. E. Viscoelasticity and molecular rheology. 2012.

(8) De Gennes, P. Dynamics of entangled polymer solutions. I. The Rouse model. *Macromolecules* **1976**, *9*, 587–593.

(9) Doi, M. Explanation for the 3.4-power law for viscosity of polymeric liquids on the basis of the tube model. *Journal of Polymer Science Polymer Physics Edition* **1983**, *21*, 667–684.

(10) Gooßen, S.; Krutyeva, M.; Sharp, M.; Feoktystov, A.; Allgaier, J.; Pyckhout-Hintzen, W.; Wischnewski, A.; Richter, D. Sensing polymer chain dynamics through ring topology: A neutron spin echo study. *Physical review letters* **2015**, *115*, 148302.

(11) Schleger, P.; Farago, B.; Lartigue, C.; Kollmar, A.; Richter, D. Clear evidence of reptation in polyethylene from neutron spin-echo spectroscopy. *Physical review letters* **1998**, *81*, 124.

(12) Wischnewski, A.; Monkenbusch, M.; Willner, L.; Richter, D.; Likhtman, A.; McLeish, T.; Farago, B. Molecular observation of contour-length fluctuations limiting topological confinement in polymer melts. *Physical review letters* **2002**, *88*, 058301.

(13) Richter, D.; Ewen, B.; Fetters, L.; Huang, J.; Farago, B. *Application of Scattering Methods to the Dynamics of Polymer Systems*; Springer, 1993; pp 130–134.

(14) Richter, D.; Farago, B.; Butera, R.; Fetters, L.; Huang, J.; Ewen, B. On the origins of entanglement constraints. *Macromolecules* **1993**, *26*, 795–804.

(15) Pyckhout-Hintzen, W.; Wischnewski, A.; Richter, D. Mixtures of polymer architectures: Probing the structure and dynamics with neutron scattering. *Polymer* **2016**, *105*, 378–392.

(16) Rao, M. A. *Rheology of fluid, semisolid, and solid foods*; Springer, 2014; pp 161–229.

(17) Chhabra, R. P.; Richardson, J. F. *Non-Newtonian flow and applied rheology: engineering applications*; Butterworth-Heinemann, 2011.

(18) Bartczak, Z. Effect of chain entanglements on plastic deformation behavior of linear polyethylene. *Macromolecules* **2005**, *38*, 7702–7713.

(19) Bartczak, Z. Effect of chain entanglements on plastic deformation behavior of ultra-high molecular weight polyethylene. *Journal of Polymer Science Part B: Polymer Physics* **2010**, *48*, 276–285.

(20) Shenoy, S. L.; Bates, W. D.; Frisch, H. L.; Wnek, G. E. Role of chain entanglements on fiber formation during electrospinning of polymer solutions: good solvent, non-specific polymer–polymer interaction limit. *Polymer* **2005**, *46*, 3372–3384.

(21) Wever, D.; Picchioni, F.; Broekhuis, A. Polymers for enhanced oil recovery: a paradigm for structure–property relationship in aqueous solution. *Progress in Polymer Science* **2011**, *36*, 1558–1628.

(22) Tsang, B.; Dell, Z. E.; Jiang, L.; Schweizer, K. S.; Granick, S. Dynamic cross-correlations between entangled biofilaments as they diffuse. *Proceedings of the National Academy of Sciences* **2017**, 201620935.

(23) June, R. K.; Mejia, K. L.; Barone, J. R.; Fyhrie, D. P. Cartilage stress–relaxation is affected by both the charge concentration and valence of solution cations. *Osteoarthritis and Cartilage* **2009**, *17*, 669–676.

(24) Han, C. D. *Rheology and Processing of Polymeric Materials: Volume 1: Polymer Rheology*; Oxford University Press on Demand, 2007; Vol. 1.

(25) Yearley, E. J.; Sasa, L. A.; Welch, C. F.; Taylor, M. A.; Kupcho, K. M.; Gilbertson, R. D.; Hjelm, R. P. The Couette configuration of the Los Alamos Neutron Science Center Neutron Rheometer for the investigation of polymers in the bulk via small-angle neutron scattering. *Review of Scientific Instruments* **2010**, *81*, 045109.

(26) Bent, J.; Hutchings, L. R.; Richards, R. W.; Gough, T.; Spares, R.; Coates, P. D.; Grillo, I.; Harlen, O. G.; Read, D. J.; Graham, R. S.; Likhtman, A. E.; Groves, D. J.; Nicholson, T. M.; McLeish, T. C. B. Neutron-Mapping Polymer Flow: Scattering, Flow Visualization, and Molecular Theory. *Science* **2003**, *301*, 1691–1695.

(27) Graham, R. S.; Bent, J.; Hutchings, L. R.; Richards, R. W.; Groves, D. J.; Embery, J.; Nicholson, T. M.; McLeish, T. C. B.; Likhtman, A. E.; Harlen, O. G.; Read, D. J.;

Gough, T.; Spares, R.; Coates, P. D.; Grillo, I. Measuring and Predicting the Dynamics of Linear Monodisperse Entangled Polymers in Rapid Flow through an Abrupt Contraction. A Small Angle Neutron Scattering Study. *Macromolecules* **2006**, *39*, 2700–2709.

(28) Clarke, N.; De Luca, E.; Buxton, G.; Hutchings, L. R.; Gough, T.; Grillo, I.; Graham, R. S.; Jagannathan, K.; Klein, D. H.; McLeish, T. C. B. Chain Deformation in Entangled Polymer Melts at Re-entrant Corners. *Macromolecules* **2010**, *43*, 1539–1542.

(29) Muller, R.; Pesce, J. J.; Picot, C. Chain conformation in sheared polymer melts as revealed by SANS. *Macromolecules* **1993**, *26*, 4356–4362.

(30) Blanchard, A.; Graham, R. S.; Heinrich, M.; Pyckhout-Hintzen, W.; Richter, D.; Likhtman, A. E.; McLeish, T. C. B.; Read, D. J.; Straube, E.; Kohlbrecher, J. Small Angle Neutron Scattering Observation of Chain Retraction after a Large Step Deformation. *Physical Review Letters* **2005**, *95*, 166001.

(31) Boué, F. *Polymer Physics*; Springer Berlin Heidelberg: Berlin, Heidelberg, 1987; pp 47–101.

(32) Kirkensgaard, J. J. K.; Hengeller, L.; Dorokhin, A.; Huang, Q.; Garvey, C. J.; Almdal, K.; Hassager, O.; Mortensen, K. Nematic effects and strain coupling in entangled polymer melts under strong flow. *Physical Review E* **2016**, *94*, 020502.

(33) Chennevière, A.; Cousin, F.; Boué, F.; Drockenmuller, E.; Shull, K. R.; Léger, L.; Restagno, F. Direct Molecular Evidence of the Origin of Slip of Polymer Melts on Grafted Brushes. *Macromolecules* **2016**, *49*, 2348–2353.

(34) Korolkovas, A.; Rodriguez-Emmenegger, C.; de los Santos Pereira, A.; Chennevière, A.; Restagno, F.; Wolff, M.; Adlmann, F. A.; Dennison, A. J. C.; Gutfreund, P. Polymer Brush Collapse under Shear Flow. *Macromolecules* **2017**, *50*, 1215–1224.

(35) Vermant, J.; Walker, L.; Moldenaers, P.; Mewis, J. Orthogonal versus parallel superposition measurements. *Journal of non-newtonian fluid mechanics* **1998**, *79*, 173–189.

(36) Watanabe, H.; Matsumiya, Y.; Inoue, T. Rheo-dielectrics in oligomeric and polymeric fluids: a review of recent findings. *Journal of Physics: Condensed Matter* **2003**, *15*, S909.

(37) Kawecki, M.; Adlmann, F. A.; Gutfreund, P.; Gupta, S.; Falus, P.; Zolnierczuk, P.; Farago, B.; Uhrig, D.; Cochran, M.; Wolff, M. Physical Review Letters (under review).

(38) Milner, S.; McLeish, T.; Likhtman, A. Microscopic theory of convective constraint release. *Journal of Rheology* **2001**, *45*, 539–563.

(39) Kremer, K.; Grest, G. S. Dynamics of entangled linear polymer melts: A molecular-dynamics simulation. *The Journal of Chemical Physics* **1990**, *92*, 5057–5086.

(40) Korolkovas, A.; Gutfreund, P.; Barrat, J.-L. Simulation of entangled polymer solutions. *The Journal of Chemical Physics* **2016**, *145*, 124113.

(41) Aoyagi, T.; Doi, M. Molecular dynamics simulation of entangled polymers in shear flow. *Computational and Theoretical Polymer Science* **2000**, *10*, 317–321.

(42) Kröger, M.; Hess, S. Rheological evidence for a dynamical crossover in polymer melts via nonequilibrium molecular dynamics. *Physical review letters* **2000**, *85*, 1128.

(43) Dorgan, J. R.; Rorrer, N. A.; Maupin, C. M. Parameter Free Prediction of Rheological Properties of Homopolymer Melts by Dynamic Monte Carlo Simulation. *Macromolecules* **2012**, *45*, 8833–8840.

(44) Halverson, J. D.; Grest, G. S.; Grosberg, A. Y.; Kremer, K. Rheology of ring polymer melts: from linear contaminants to ring-linear blends. *Physical review letters* **2012**, *108*, 038301.

(45) Padding, J.; Briels, W. Coarse-grained molecular dynamics simulations of polymer melts in transient and steady shear flow. *The Journal of chemical physics* **2003**, *118*, 10276–10286.

(46) Xu, X.; Chen, J.; An, L. Shear thinning behavior of linear polymer melts under shear flow via nonequilibrium molecular dynamics. *The Journal of chemical physics* **2014**, *140*, 174902.

(47) Cao, J.; Likhtman, A. E. Simulating startup shear of entangled polymer melts. *ACS Macro Letters* **2015**, *4*, 1376–1381.

(48) Huang, C.-C.; Gompper, G.; Winkler, R. G. Non-equilibrium properties of semidilute polymer solutions under shear flow. Journal of Physics: Conference Series. 2012; p 012003.

(49) Korolkovas, A. Simulation of long polymer chains under shear flow. 2017; `https://doi.org/10.5281/zenodo.439529`.

(50) Lees, A.; Edwards, S. The computer study of transport processes under extreme conditions. *Journal of Physics C: Solid State Physics* **1972**, *5*, 1921.

(51) de Gennes, P. G. *Scaling Concepts in Polymer Physics*; Cornell University Press, 1979.

(52) Bolhuis, P.; Louis, A.; Hansen, J.; Meijer, E. Accurate effective pair potentials for polymer solutions. *The Journal of Chemical Physics* **2001**, *114*, 4296–4311.

(53) Karayiannis, N. C.; Kröger, M. Combined molecular algorithms for the generation, equilibration and topological analysis of entangled polymers: Methodology and performance. *International journal of molecular sciences* **2009**, *10*, 5054–5089.

(54) Hsu, H.-P.; Kremer, K. Detailed analysis of Rouse mode and dynamic scattering function of highly entangled polymer melts in equilibrium. *arXiv preprint arXiv:1701.02702* **2017**,

(55) Bruzzone, S.; Malvaldi, M. Dynamics of relaxation of entangled polymers in shear flow. *The Journal of chemical physics* **2006**, *125*, 064909.

(56) Noirez, L.; Mendil-Jakani, H.; Baroni, P. New Light on Old Wisdoms on Molten Polymers: Conformation, Slippage and Shear Banding in Sheared Entangled and Unentangled Melts. *Macromolecular Rapid Communications* **2009**, *30*, 1709–1714.

(57) Kawecki, M.; Gutfreund, P.; Adlmann, F.; Lindholm, E.; Longeville, S.; Lapp, A.; Wolff, M. Probing the dynamics of high-viscosity entangled polymers under shear using Neutron Spin Echo spectroscopy. Journal of Physics: Conference Series. 2016; p 012014.

(58) Wolff, M.; Magerl, A.; Frick, B.; Zabel, H. Dynamics and structure in complex liquids under shear explored by neutron scattering. *Physical Review E* **2005**, *71*, 011509.

(59) Kim, S.; Mewis, J.; Clasen, C.; Vermant, J. Superposition rheometry of a wormlike micellar fluid. *Rheologica Acta* **2013**, *52*, 727–740.

(60) Leclaire, S.; El-Hachem, M.; Trépanier, J.-Y.; Reggio, M. High order spatial generalization of 2D and 3D isotropic discrete gradient operators with fast evaluation on GPUs. *Journal of Scientific Computing* **2014**, *59*, 545–573.

(61) Kobayashi, H.; Yamamoto, R. Implementation of Lees–Edwards periodic boundary conditions for direct numerical simulations of particle dispersions under shear flow. *The Journal of chemical physics* **2011**, *134*, 064110.